Cell Reports
Methods

Article

Human *MAPT* knockin mouse models of frontotemporal dementia for the neurodegenerative research community

Graphical abstract

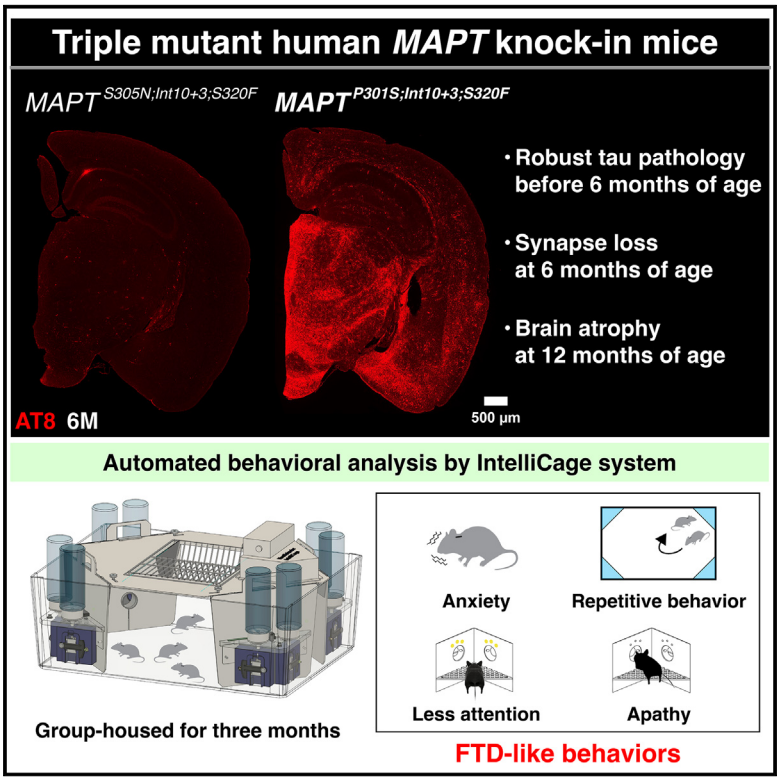

Highlights

- Three *MAPT* pathogenic mutations are introduced into human *MAPT* knockin mice
- We establish a line with abnormal tau accumulation before 6 months
- Aberrant tau deposition leads to synaptic loss, brain atrophy, and FTD-like behaviors
- The triple mutant *MAPT* knockin mouse is a model for tau-targeted drug screening

Authors

Takahiro Morito, Mohan Qi, Naoko Kamano, ..., Makoto Higuchi, Takaomi C. Saido, Naoto Watamura

Correspondence

takaomi.saido@riken.jp (T.C.S.), naoto.watamura@a.riken.jp (N.W.)

In brief

Morito et al. present human *MAPT* knockin mice harboring three pathogenic mutations associated with frontotemporal dementia (FTD). One of the mutant lines exhibits robust tau pathology before 6 months of age, leading to FTD-like behavioral abnormalities. These mice serve as valuable models for FTD drug screening and are available to researchers worldwide.

Morito et al., 2025, Cell Reports Methods *5*, 101024
April 21, 2025
https://doi.org/10.1016/j.crmeth.2025.101024

CellPress

Cell Reports Methods

CellPress
OPEN ACCESS

Article

Human *MAPT* knockin mouse models of frontotemporal dementia for the neurodegenerative research community

Takahiro Morito,[1,8] Mohan Qi,[1,8] Naoko Kamano,[1] Hiroki Sasaguri,[1,2] Sumi Bez,[3] Martha Foiani,[3] Karen Duff,[3] Seico Benner,[4] Toshihiro Endo,[5] Hiroshi Hama,[6] Hiroshi Kurokawa,[6] Atushi Miyawaki,[6] Hiroshi Mizuma,[7] Naruhiko Sahara,[7] Masafumi Shimojo,[7] Makoto Higuchi,[7] Takaomi C. Saido,[1,9,*] and Naoto Watamura[1,3,*]

[1]Laboratory for Proteolytic Neuroscience, RIKEN Center for Brain Science, Wako, Saitama 351-0198, Japan
[2]Dementia Pathophysiology Collaboration Unit, RIKEN Center for Brain Science, Wako, Saitama 351-0198, Japan
[3]UK Dementia Research Institute, University College London, London WC1E6BT, UK
[4]Center for Health and Environmental Risk Research, National Institute for Environmental Studies, Tsukuba, Ibaraki 305-8506, Japan
[5]Phenovance LLC, Kashiwa, Chiba 277-0882, Japan
[6]Laboratory for Cell Function Dynamics, RIKEN Center for Brain Science, Wako, Saitama 351-0198, Japan
[7]Advanced Neuroimaging Center, National Institutes for Quantum Science and Technology, Inage, Chiba 263-8555, Japan
[8]These authors contributed equally
[9]Lead contact
*Correspondence: takaomi.saido@riken.jp (T.C.S.), naoto.watamura@a.riken.jp (N.W.)
https://doi.org/10.1016/j.crmeth.2025.101024

MOTIVATION The accumulation of pathological tau is a hallmark of neurodegenerative diseases such as frontotemporal dementia (FTD) and Alzheimer's disease. While mouse models have been instrumental in studying tau-mediated neurodegeneration, existing models largely rely on the artificial overexpression of mutant tau proteins, which may not fully recapitulate disease pathology. To address this limitation, we recently developed human *MAPT* knockin mice carrying single- or double-pathogenic MAPT mutations associated with FTD. Among these, the *MAPT*$^{S305N;Int10+3}$ mouse exhibits tau pathology and concurrent behavioral abnormalities at approximately 14 months of age. To generate more pathophysiologically relevant and user-friendly FTD models, we developed triple-mutant *MAPT* knockin mice and characterized their potential as tools for studying tau-mediated neurodegeneration.

SUMMARY

Existing models of frontotemporal dementia (FTD) may not fully recapitulate the pathophysiology of the disease. To generate more pathophysiologically relevant FTD models, we engineered *MAPT* knockin mouse lines carrying triple mutations, among which the *MAPT*$^{P301S;Int10+3;S320F}$ line exhibited robust tau pathology starting before 6 months of age. Severe tau accumulation was predominantly observed in the thalamus, hypothalamus, and amygdala with milder involvement of the cortex and hippocampus, leading to synaptic loss, brain atrophy, and FTD-like behavioral abnormalities. Crossbreeding *MAPT*$^{P301S;Int10+3;S320F}$ mice with *App* knockin, *App*$^{NL-G-F}$, mice markedly enhanced tau pathology in the cortex and hippocampus, highlighting the interplay between β-amyloid and tau. These findings establish the mutant mice as valuable models for investigating the mechanisms underlying FTD and other tauopathies, providing a relevant platform for *in vivo* drug screening.

INTRODUCTION

Mutations in the coding and non-coding regions of the human *MAPT* gene are known to cause a form of frontotemporal dementia (FTD).[1] Accumulation of hyperphosphorylated tau in the brain represents the major pathological hallmark of FTD and parkinsonism linked to chromosome 17 (FTDP-17). We previously introduced FTD-causing pathogenic mutations into human *MAPT* knockin (KI) mice[2,3] using cytosine base editor (BE),[4] which resulted in the generation of seven isogenic mutant KI mouse lines.[5] Utilizing KI mice rather than transgenic overexpression mice is beneficial for modeling diseased conditions while avoiding overexpression artifacts such as the destruction of endogenous loci, disturbances in cellular protein localization/interactions, and non-specific endoplasmic reticulum stress/calcium mobilization.[6–12] Another major drawback of the overexpression paradigm is the inapplicability

of genome editing because multiple copies of cDNA(s) are usually inserted into the host genome in a random manner.[13]

Of the seven lines mentioned above, we had performed detailed immunochemical and biochemical analyses of two KI lines: a single Intron10+3 G>A mutant and a double S305N-Intron10+3 G>A mutant (*MAPT*$^{Int10+3}$ and *MAPT*$^{S305N;Int10+3}$). Both of these lines exhibited alterations in *MAPT* pre-mRNA splicing and a significant increase in 4-repeat (4R) tau isoforms with a concomitant decrease in 3-repeat (3R) isoforms, resulting in the hyperphosphorylation of tau.[5] These mutant mice presented pathological deposition of hyperphosphorylated tau accompanying synaptic loss and cognitive impairment at the age of 15 months or later, but they failed to show accumulation of seed-competent tau oligomers as in human cases. We also created another double mutant *MAPT* KI mouse, *MAPT*$^{P301S;Int10+3}$, but this line also showed almost no histopathological phenotype until 24 months of age unless crossbred with *App* KI mice.[11] Mouse models that exhibit more rapid and severe pathological and behavioral changes should be valuable tools for studying tauopathies with KI mouse models.

To generate pathophysiologically more relevant and user-friendly models of FTD, we added another pathogenic mutation, S320F, to *MAPT*$^{S305N;Int10+3}$ and *MAPT*$^{P301S;Int10+3}$ mice. This mutation, present in exon 11 of the *MAPT* gene, is known to affect the structural properties of tau rather than the alternative splicing of its pre-mRNA.[14–17] These efforts resulted in the generation of the new triple mutant lines, *MAPT*$^{P301S;Int10+3;S320F}$, *MAPT*$^{S305N;Int10+3;S320F}$, and *MAPT*$^{S305N;Int10+3;S320Y}$.

We here describe the pathological, biochemical, and behavioral phenotypes of the triple-mutant KI lines. Among the three, the *MAPT*$^{P301S;Int10+3;S320F}$ line exhibited typical FTD-like pathology accompanying hyperphosphorylated oligomeric tau formation together with synaptic loss earlier than 6 months of age. We also observed local brain atrophy, FTD-like behavioral abnormality, and an increase in body weight at a later age. Accordingly, these next-generation mouse models of FTD should be suitable for use in preclinical studies to understand the disease mechanisms and to search for therapeutic candidates for FTD and Alzheimer's disease (AD) with minimal concerns about overexpression artifacts in both *in vivo* and *in vitro* contexts.

RESULTS

Generation of mutant *MAPT* KI mice harboring three FTD-causing mutations

We previously created two mouse lines that carry S305N/Intron10+3 G>A mutations (*MAPT*$^{S305N;Int10+3}$) or P301S/Intron10+3 G>A mutations (*MAPT*$^{P301S;Int10+3}$) using cytosine BE.[4,5,11] Because an S320F mutation has been reported to accelerate aggregation of tau protein in combination with P301 mutations,[14,17] we added this mutation to the double mutants by designing a single guide RNA (sgRNA) targeting the S320 position, with -NGG protospacer adjacent motif (PAM) sequences for BE-mediated genome editing. The sgRNA and cytosine BE mRNA were microinjected into the zygotes from *MAPT*$^{S305N;Int10+3}$ and *MAPT*$^{P301S;Int10+3}$ mice, and they were individualized to obtain triple-mutant mice. We successfully introduced an S320F mutation to *MAPT*$^{S305N;Int10+3}$ and *MAPT*$^{P301S;Int10+3}$ mice in the second-round genome editing, thereby obtaining the following lines: *MAPT*$^{S305N;Int10+3}$ mice with the S320F mutation (*MAPT*$^{S305N;Int10+3;S320F}$) and *MAPT*$^{P301S;Int10+3}$ mice with the S320F mutation (*MAPT*$^{P301S;Int10+3;S320F}$) (Figures 1A–1C). After the second editing, we confirmed the absence of any potential off-target mutations by *in silico* homology analysis with whole-genome resequencing data.[18] After backcrossing the mutants with wild-type B6/J mice three times or more, we obtained homozygous *MAPT*$^{S305N;Int10+3;S320F}$ and *MAPT*$^{P301S;Int10+3;S320F}$ mice. All mice described in this paper are homozygotes. Presumably due to the random nature of BE, we also obtained *MAPT*$^{S305N;Int10+3}$ mice carrying the S320Y mutation (*MAPT*$^{S305N;Int10+3;S320Y}$). The other mutants generated during these procedures included the following: the double *MAPT*-Intron10+3 G>A plus S320F mutation (*MAPT*$^{Int10+3;S320F}$), *MAPT*-P301L plus S320F mutation (*MAPT*$^{P301L;S320F}$), and the single *MAPT*-S320F mutation (*MAPT*^{S320F}) (Figure S1). We list the mutant mouse lines in Table S1. Off-target candidate sites for the introduction of S320F are shown in Table S2.

Expression pattern of tau isoforms in triple-mutant *MAPT* KI mice

To investigate the expression pattern of tau isoforms, we performed western blot analysis using brain homogenates from cortices of each mouse line after dephosphorylation treatment (Figure 1D). The expression of 3R tau was undetectable in *MAPT*$^{S305N;Int10+3;S320F}$ mice. In contrast, the *MAPT*$^{P301S;Int10+3;S320F}$ line produced a small but detectable quantity of 3R tau, the 0N3R isoform in particular (Figure 1E). Accordingly, the 4R tau was highly expressed in the *MAPT*$^{S305N;Int10+3;S320F}$ mice, and the *MAPT*$^{P301S;Int10+3;S320F}$ mice expressed much more 4R than 3R tau isoforms (Figure 1E). These results are consistent with RT-PCR showing that 3R tau transcripts were absent in *MAPT*$^{S305N;Int10+3;S320F}$ mice and minimally present in *MAPT*$^{P301S;Int10+3;S320F}$ mice (Figures 1F and 1G). Likewise, a small amount of 3R tau transcripts was detected in *MAPT*$^{P301S;Int10+3;S320F}$mice and absent in *MAPT*$^{S305N;Int10+3;S320F}$ mice in the real-time PCR analysis, whereas the total tau expression levels were comparable among all groups (Figure 1H). We also observed similar pattens of 3R/4R tau ratios in the *MAPT*$^{S305N;Int10+3;S320F}$ and *MAPT*$^{S305N;Int10+3;S320Y}$ mice (Figures S2A-S2D). These results indicate that the 10+3 G>A intronic mutation affects the alternative splicing, causing a shift from 3R to 4R tau even in the presence of other mutations, and that the S305N mutation strengthens this effect in a manner described previously.[5]

Spatiotemporal mapping of AT8-positive phosphorylated tau accumulation

We conducted immunofluorescence staining with the AT8 antibody, which detects phosphorylation of tau at Ser202 and Thr205, on four different coronal sections (from anterior to posterior) to investigate the distribution of phosphorylated tau. The heatmaps created by the intensity of AT8-positive signals revealed the strongest tau pathology in the hypothalamus and amygdala with relatively less intensity in the somatosensory and auditory cortices in addition to the hippocampus in *MAPT*$^{P301S;Int10+3;S320F}$mice at the age of 6 months

CellPress
OPEN ACCESS

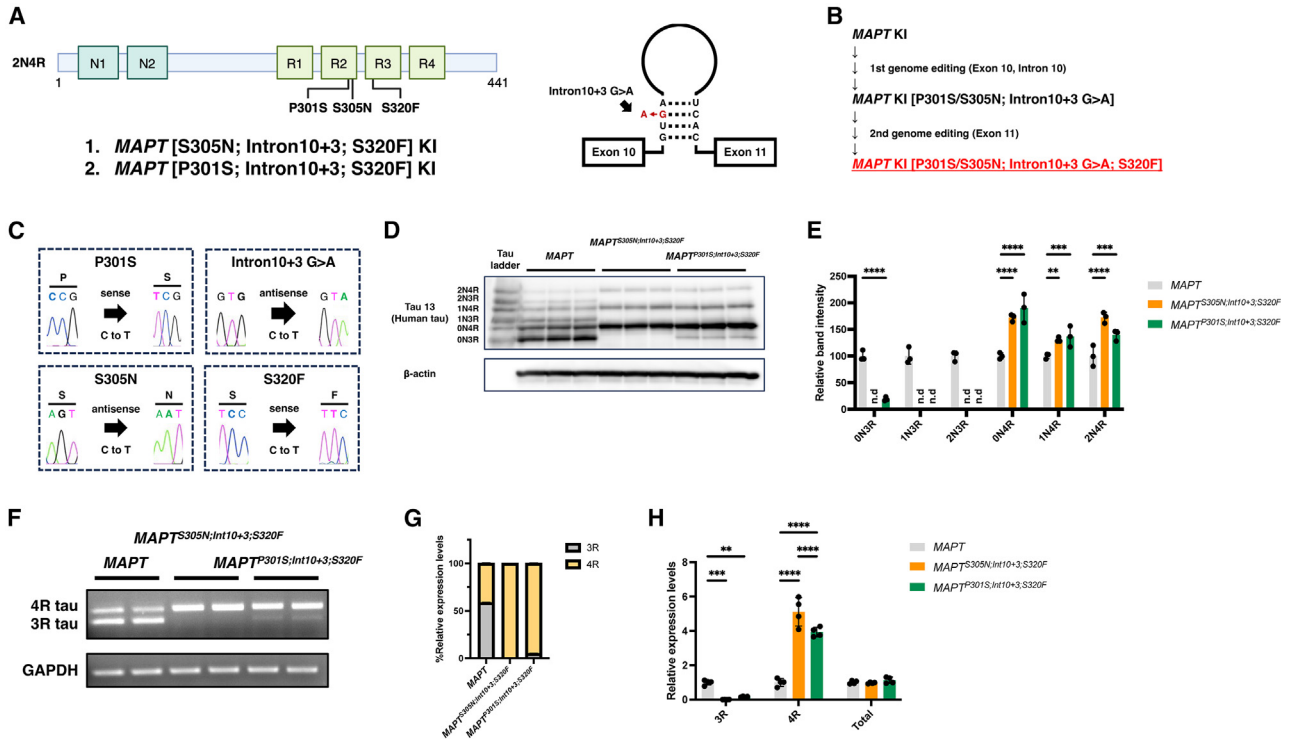

Figure 1. Generation and tau isoform expression patterns of triple-mutant *MAPT* KI mouse lines

(A) Schematic of pathogenic mutations in the human *MAPT* gene, showing mutations in the exon (left) and intron (right).

(B) Workflow of the two genome editing steps for generating *MAPT*$^{S305N;Int10+3;S320F}$ and *MAPT*$^{P301S;Int10+3;S320F}$ mice.

(C) Four pathogenic mutations introduced by base editing.

(D and E) Western blot analysis of alkaline phosphatase-treated tau protein from the frontal cortices of *MAPT*, *MAPT*$^{S305N;Int10+3;S320F}$, and *MAPT*$^{P301S;Int10+3;S320F}$ mice at the age of 6 months (D) and densitometric quantification of each isoform (E) (n = 3 per group, 2 males and 1 female).

(F and G) RT-PCR analysis of the *MAPT* gene transcripts from the frontal cortices of *MAPT*, *MAPT*$^{S305N;Int10+3;S320F}$, and *MAPT*$^{P301S;Int10+3;S320F}$ mice at the age of 6 months using primer sets specific for 3R tau, 4R tau, and GAPDH (F) and densitometry quantification (G) (n = 4 per group, 2 males and 2 females).

(H) Quantitative real-time PCR analysis of the *MAPT* gene transcripts from the frontal cortices of *MAPT*, *MAPT*$^{S305N;Int10+3;S320F}$, and *MAPT*$^{P301S;Int10+3;S320F}$ mice at the age of 6 months (n = 4 per group, 2 males and 2 females).

In (E) and (H), the data are presented as mean ± SD (two-way ANOVA with Tukey's multiple comparison test). $^{**}p < 0.01$, $^{***}p < 0.005$, $^{****}p < 0.001$. n.d., not detected. See also Figures S1 and S2 and Table S2.

(Figures 2A–2C). We also observed intense AT8-positive signals in the piriform cortex and thalamus. The *MAPT*$^{S305N;Int10+3;S320F}$ mice showed a similar pattern of AT8-positive signals with a lower intensity (Figures 2A and 2C). The accumulation of phosphorylated tau increased progressively (and almost linearly) in an age-dependent manner in *MAPT*$^{P301S;Int10+3;S320F}$ mice (Figures 2D and 2E). Although it is not possible to determine the age of onset in pathological terms, extrapolation of the data shown in Figure 2E implies that tau accumulation is likely to start at 4–5 months of age or even earlier, particularly in the hypothalamus. *MAPT*$^{S305N;Int10+3;S320Y}$ mice also showed phosphorylated tau accumulation in the hypothalamus and amygdala, in particular at the age of 6 months, but the extent of tau pathology was less than that of the *MAPT*$^{P301S;Int10+3;S320F}$mice (Figure S2E).

Histological studies of tau pathology using various tau antibodies

To assess the pathological status of tau protein in the triple-mutant *MAPT* KI mouse lines, we performed immunofluorescence analysis using a panel of antibodies that recognize the phosphorylated, oligomeric, and pathological conformation structure of tau protein (Figure 3A). Immunohistochemistry using CP13 (pS202), PHF-1 (pS396/S404), TOC1, T22, and MC1[19–23] antibodies clearly highlighted the presence of hyperphosphorylated and oligomeric/conformationally abnormal tau in the brain of *MAPT*$^{P301S;Int10+3;S320F}$ mice (Figures 3A and 3B). With the identical panel of antibodies, we observed less intense and milder signals in *MAPT*$^{S305N;Int10+3;S320F}$ and *MAPT*$^{S305N;Int10+3;S320Y}$ mice (Figures 3B and S2F). These results were consistent with those seen in 3,3′diaminobenzidine staining (Figure S3). The AT8 immunoreactivity colocalized with MAP2 and kinesin immunoreactivities (Figure 3C), indicating the presence of phosphorylated tau in the neuronal dendrites, somata, and axons.

Biochemical analysis of tau pathology in triple-mutant *MAPT* KI mice

Sarkosyl fractionation has been employed to isolate pathological tau proteins from bulk brain tissues.[24] Through this method, we

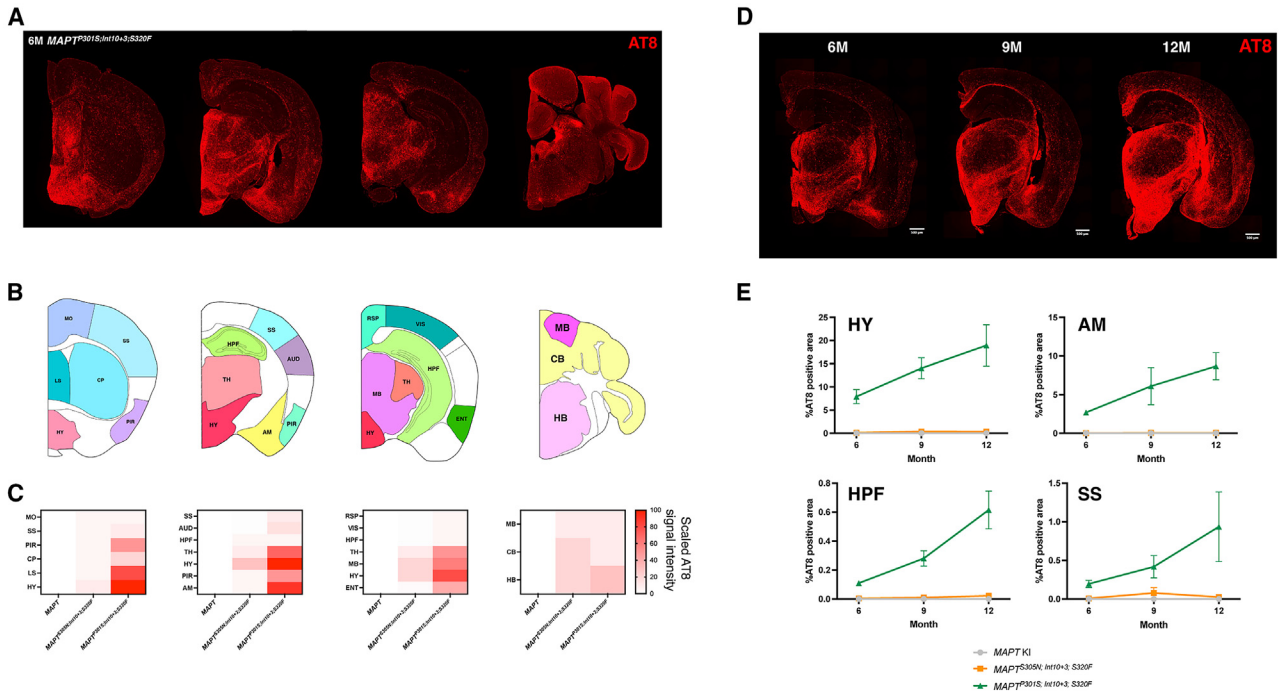

Figure 2. Spatiotemporal mapping of tau pathology in triple-mutant *MAPT* KI mouse lines

(A) Representative coronal sections of 6-month-old *MAPT*$^{P301S;Int10+3;S320F}$ mice, stained with the AT8 antibody. Scale bar: 500 μm.

(B) Schematic of several brain regions used for creating the heatmaps. MO, somatomotor area; SS, somatosensory area; PIR, piriform area; CP, caudoputamen; LS, lateral septal nucleus; HY, hypothalamus; AUD, auditory area; HPF, hippocampal formation; TH, thalamus; AM, amygdala; RSP, retrosplenial area; VIS, visual area; MB, midbrain; ENT, entorhinal area; CB, cerebellum; HB, hindbrain.

(C) Heatmaps of AT8 immunopositivity in different brain regions for *MAPT*, *MAPT*$^{S305N;Int10+3;S320F}$, and *MAPT*$^{P301S;Int10+3;S320F}$ mice at the age of 6 months. At least four biological replicates (2 males and 2 females) were used for creating the heatmap.

(D) Representative AT8 immunostained brain slice images of male *MAPT*$^{P301S;Int10+3;S320F}$ mice at 6, 9, and 12 months of age. Scale bar: 500 μm.

(E) Time curves of AT8 immunopositivity for *MAPT*, *MAPT*$^{S305N;Int10+3;S320F}$, and *MAPT*$^{P301S;Int10+3;S320F}$ mice at HY, AM, HPF, and SS (n = 4 per genotype and age, 2 males and 2 females).

All immunostaining images were acquired simultaneously under consistent contrast settings. The data are presented as mean ± SD.

obtained Tris-buffered saline (TBS)-soluble fractions (S1), which contained physiological forms of tau, and sarkosyl-insoluble fractions (P3), which contained pathological forms of tau (i.e., tau protein with an oligomerization-prone conformation) from frozen thalamus/hypothalamus brain tissue (Figure 4A). In the S1 fractions, the expression level of total tau, represented by Tau13 antibody, showed distinct band patterns in the two mutant lines compared to wild-type human *MAPT* KI (Figure 4B). However, the densitometry analysis showed that the amount of total tau was equivalent across genotypes (Figures 4B and 4C). Intriguingly, phosphorylation levels of tau, detected by AT8, CP13, and PHF-1 antibodies, were significantly lower in *MAPT*$^{S305N;Int10+3;S320F}$ and *MAPT*$^{S305N;Int10+3;S320Y}$ mice compared to the *MAPT* KI (Figures 4B, 4C, S2G, and S2H). Furthermore, sarkosyl-insoluble phosphorylated tau was detectable in *MAPT*$^{P301S;Int10+3;S320F}$ and *MAPT*$^{S305N;Int10+3;S320Y}$ mice (Figures 4D and S2I). We also analyzed S1 and P3 fractions from cortical frozen brain tissues and found lower phosphorylation levels of tau in *MAPT*$^{S305N;Int10+3;S320F}$ and *MAPT*$^{P301S;Int10+3;S320F}$ mice compared with *MAPT* KI mice (Figures S4A and S4B). Meanwhile, the P3 fraction from *MAPT*$^{P301S;Int10+3;S320F}$ mice also contained AT8-positive sarkosyl-insoluble tau species, indicating the presence of highly oligomer-prone features of tau in *MAPT*$^{P301S;Int10+3;S320F}$ mice (Figure S4C).

To assess whether tau from triple *MAPT* KI mutants is capable of forming self-replicating assemblies (seeds), we employed biosensor cell lines overexpressing the repeat domain of tau containing the P301S mutation tagged with cyan fluorescent protein (CFP) or yellow fluorescent protein (YFP) (Figure 4E).[26] The brain lysates of S1 or P3 fractions from the hypothalamus and cortex in *MAPT*$^{P301S;Int10+3;S320F}$ significantly increased seeding activity in these biosensor cells (Figures 4F, 4G, S4D, and S4E), showing the presence of a pathological seed-competent conformation of tau comparable to that of the 12-month-old PS19 line,[27] even at the age of 6 months.

Neuroinflammation, synaptic loss, and neurodegeneration

Neuroinflammation and synaptic loss are characterized as pathological hallmarks of AD and other tauopathies.[28,29] We thus performed immunohistochemistry of glial fibrillary acidic protein (GFAP) and Iba1 to assess neuroinflammation and found a significant upregulation of GFAP and no alterations in Iba1

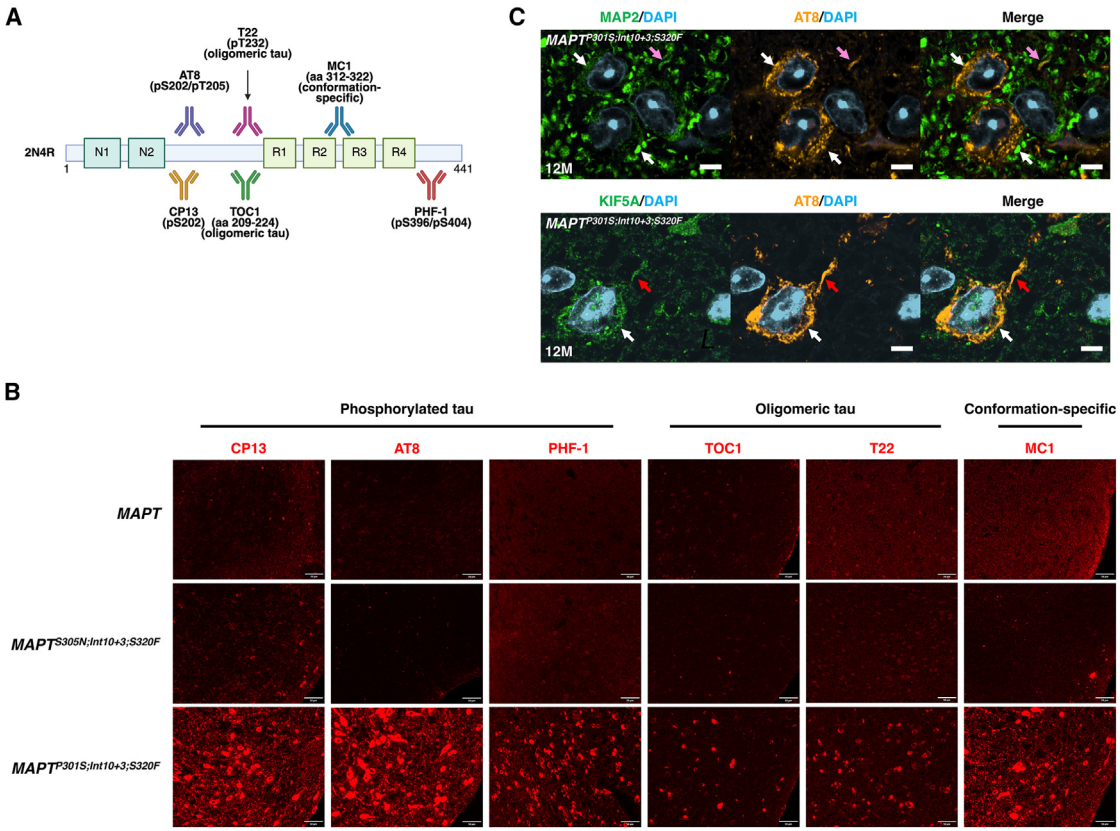

Figure 3. Immunohistochemical analysis of triple-mutant *MAPT* KI mouse lines

(A) Epitope maps of anti-tau antibodies used for this study.

(B) Immunohistochemical analysis of HY of male *MAPT*, *MAPT*$^{S305N;Int10+3;S320F}$, and *MAPT*$^{P301S;Int10+3;S320F}$ mice at the age of 6 months using CP13, AT8, PHF-1, TOC1, T22, and MC1 antibodies. Scale bars: 50 μm; $n = 4$ (2 males and 2 females).

(C) Colocalization of AT8 signals with MAP2 (a marker for somata and dendrites, top) or KIF5A (a marker for somata and axons, bottom) in the cortical region of 12-month-old *MAPT*$^{P301S;\ Int10+3;\ S320F}$ mice. Scale bars: 5 μm. Pink, white, and red arrows indicate dendrite, soma, and axon, respectively.

See also Figure S3.

immunoreactivity (Figures 5A–5C). These results indicate that microgliosis is not proportionally exerted by tau accumulation, showing a reduced association between tau pathology and microglia in these models, at least at 12 months of age.

Next, we analyzed the synaptic integrity using super-resolution confocal microscopy. Colocalization of synaptic puncta detected by synaptotagmin, a pre-synaptic marker, and Homer1, a post-synaptic marker, was significantly decreased in the hypothalamus of *MAPT*$^{P301S;Int10+3;S320F}$ compared with those in *MAPT* mice (Figures 5D and 5E). No alterations in synaptic density in the piriform cortices, which are relatively preserved from tau pathology, were seen in *MAPT*$^{P301S;Int10+3;S320F}$ mice (Figure S5). We also performed western blot analysis of the pre- and post-synaptic markers synaptophysin, synaptotagmin, and PSD-95. A significant reduction in the expression levels of both synaptophysin and synaptotagmin was observed in *MAPT*$^{P301S;Int10+3;S320F}$ compared with those in *MAPT* mice, whereas the amount of PSD-95 remained equivalent among the three groups in the thalamic/hypothalamic fractions of brain extracts (Figure 5F). These findings suggest that the pre-synapse is more susceptible to tau pathology than the post-synapse.

We then performed Gallyas silver staining to detect signs of neurodegeneration in these brain sections. Staining-positive cells were observed in the hypothalamus of 12-month-old *MAPT*$^{P301S;Int10+3;S320F}$ mice, consistent with findings in PS19 mice (Figure 5G).

We subsequently conducted magnetic resonance imaging (MRI) analysis to evaluate brain atrophy. Control images, which were obtained by averaging five *MAPT* control brain images, were divided into 20 sections, and five representative brain regions (cortex, hippocampus, thalamus, hypothalamus, and amygdala) were selected for comparison of brain volumes with mutant mice (Figures 5H and S6A–S6E). Of those regions, the hypothalamus and amygdala brain volumes were significantly diminished in *MAPT*$^{S305N;Int10+3;S320F}$ and *MAPT*$^{P301S;Int10+3;S320F}$ mice in comparison with *MAPT* control mice, indicating tau pathology-driven local brain atrophy in the hypothalamus and amygdala (Figures 5I and S6B). Additionally, a significant reduction in hippocampal volumes was also detectable in *MAPT*$^{P301S;Int10+3;S320F}$ mice.

In summary, GFAP is upregulated in the hypothalamus without changes to Iba1 immunopositivity, demonstrating the relevance

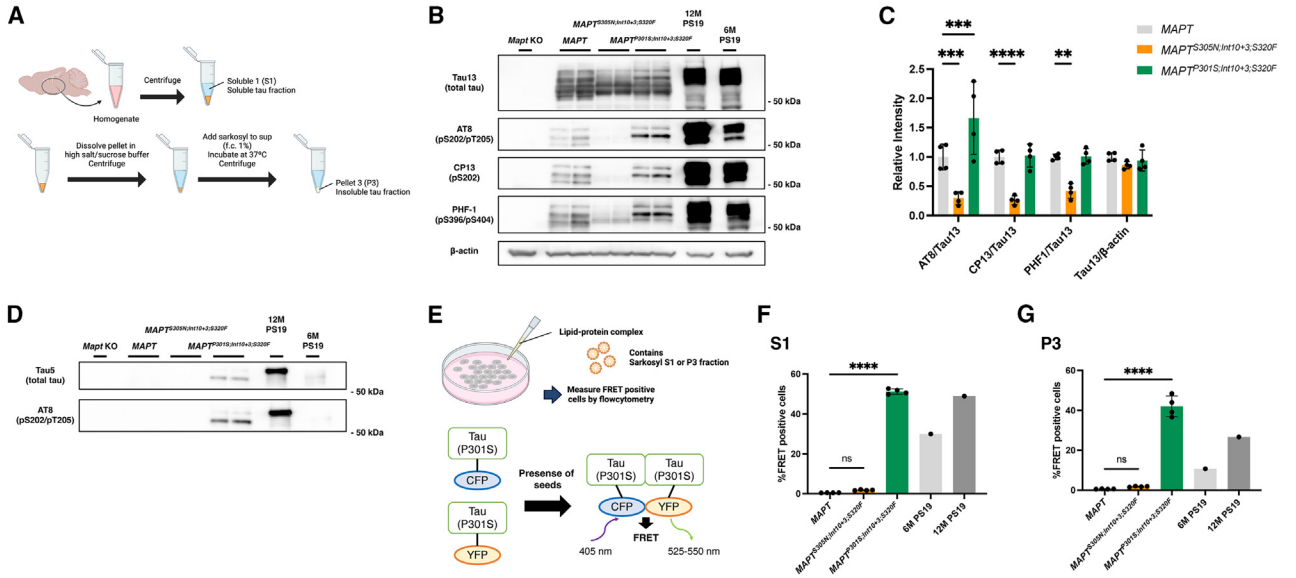

Figure 4. Sarkosyl fractionation of tau from brain extracts and their seeding potency, analyzed by tau biosensor cells

(A) A schematic of sarkosyl fractionation of tau. Sup, supernatant.

(B and C) Western blot analyses of TBS-soluble fractions from the TH of *MAPT*, *MAPT*$^{S305N;Int10+3;S320F}$, and *MAPT*$^{P301S;Int10+3;S320F}$ mice at the age of 6 months (n = 4 per group, 2 males and 2 females) and PS19 at the age of 6 and 12 months using Tau13, AT8, CP13, and PHF-1 antibodies (B) and densitometry quantification (C). A *Mapt* knockout mouse was used as a negative control, and PS19 mice were used as positive controls.

(D) Western blot analyses of sarkosyl-insoluble fractions from the TH of *MAPT*, *MAPT*$^{S305N;Int10+3;S320F}$, and *MAPT*$^{P301S;Int10+3;S320F}$ mice at the age of 6 months using Tau5 and AT8 antibodies (n = 4 per group, 2 males and 2 females).

(E) Schematic of the tau seeding assay using tau biosensor cells.

(F and G) The percentage of fluorescence resonance energy transfer-positive cells 48 h after incubation with S1 (F) or P3 (G) fractions from the TH of *MAPT*, *MAPT*$^{S305N;Int10+3;S320F}$, and *MAPT*$^{P301S;Int10+3;S320F}$ mice at the age of 6 months (n = 4 per group, 2 males and 2 females) and PS19 mice at the age of 6 and 12 months, using biosensor cells.[25]

In (C), the data are presented as the mean ± SD (two-way ANOVA with Tukey's multiple comparison test). $^{**}p < 0.01$, $^{***}p < 0.005$, $^{****}p < 0.001$. In (F) and (G), the data are presented as the mean ± SD (one-way ANOVA with Tukey's multiple comparison test). $^{****}p < 0.001$. See also Figure S4.

of astrogliosis with abnormal tau. Accumulated Gallyas-positive signals in the hypothalamus in addition to synaptic loss and atrophy can be detected, indicating region-specific pathological tau-mediated neurodegeneration of *MAPT*$^{P301S;Int10+3;S320F}$ mice in a manner consistent with the observations from MRI analysis.

Behavioral analyses using the IntelliCage system

The IntelliCage system is an automated apparatus for analyzing various cognitive behaviors for group-housed mice.[30–33] It contains four conditioning corners with two nosepoke holes each with a gate to access the drinking water spout (Figure 6A). This system automatically records access to the conditioning corners, nosepoking, and water licking of each mouse. Behaviors in three mouse lines—*MAPT* (control), *MAPT*$^{S305N;Int10+3;S320F}$, and *MAPT*$^{P301S;Int10+3;S320F}$—were analyzed. To assess whether the mutant lines have face validity as models of dementia, especially with tauopathy, we investigated the signs of (1) altered emotional responses, (2) repetitive/stereotypical behavior, (3) impairments in learning and behavioral flexibility, (4) impairments in behavioral inhibition and sustained attention, and (5) anhedonia and apathy.

First, to assess the signs of altered emotional response of the mice, we analyzed their activity during the 24 h after the mice were placed in the IntelliCage for the first time (Figure 6B). *MAPT*$^{P301S;Int10+3;S320F}$ mice exhibited a significant decrease in the total number of licking bouts compared to *MAPT* control mice during the first 24 h. The reduction was interpreted as a sign of elevated anxiety due to the exposure to a novel environment, as the same index in the following 14 days did not differ among groups (Figure 6C).

Second, we analyzed the signs of repetitive/stereotypical behavior. The corner preference and side preference of mutant mice were indistinguishable those of from controls (Figure S7A). However, the percentage of re-entering the same corner in all patterns of corner-to-corner movements was significantly increased in *MAPT*$^{P301S;Int10+3;S320F}$ mice during the 14 days (Figure 6D). This was a sign of repetitive/stereotypical behavior, which is one of the clinical features of FTD (Figure 6D).[34]

Third, to assess the ability of learning and behavioral flexibility, we conducted a task called the self-paced learning and behavioral flexibility.[35] In this test, mice were required to learn a sequence of moving back and forth between two distant rewarding corners of four corners and adapt to the subsequent serial rule shifts. For each individual, whenever the correct response rate reached a criterion (30%), the rewarding corners changed (i.e., rule shift). The number of trials to reach the criterion for the rule shift was used as the performance index. No

CellPress
OPEN ACCESS

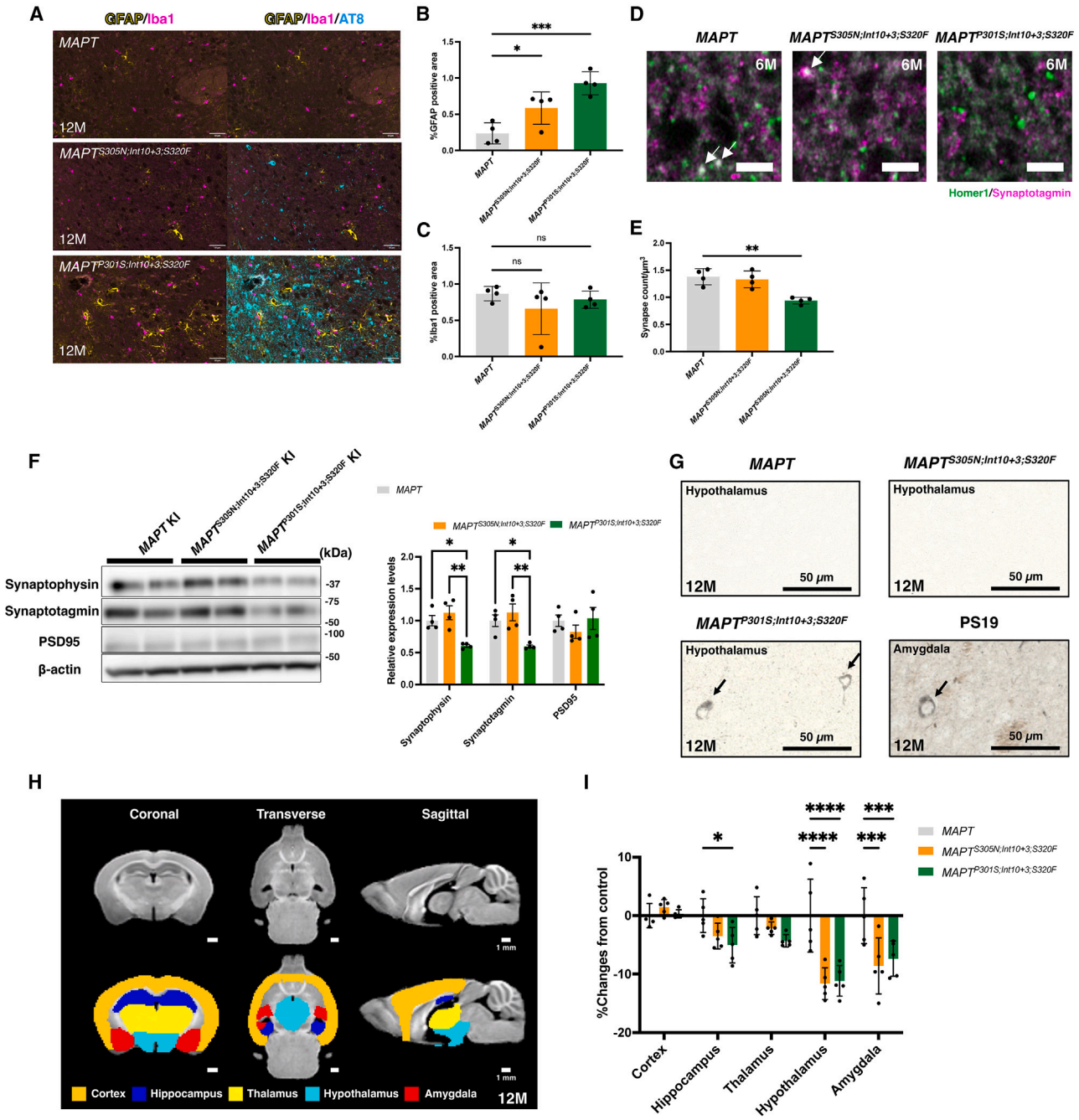

Figure 5. Neuroinflammation, synaptic loss, and neurodegeneration in triple-mutant *MAPT* KI mice

(A–C) GFAP and Iba1 immunohistochemistry to assess neuroinflammation (A) and quantification of immuno-positive signals in the HY of 12-month-old *MAPT*, *MAPT*$^{S305N;Int10+3;S320F}$, and *MAPT*$^{P301S;Int10+3;S320F}$ mice (n = 4 per group, 2 males and 2 females). Scale bars: 50 μm (B and C).

(D and E) Representative super-resolution images of synaptotagmin and Homer1 punctum colocalization in the HY of 6-month-old *MAPT*, *MAPT*$^{S305N;Int10+3;S320F}$, and *MAPT*$^{P301S;Int10+3;S320F}$ lines (D) and quantification of synaptotagmin/Homer1 colocalization density in the HY of 6-month-old *MAPT*, *MAPT*$^{S305N;Int10+3;S320F}$, and *MAPT*$^{P301S;Int10+3;S320F}$ mice (n = 4 per group, 2 males and 2 females) (E). White arrows indicate colocalized signals.

(F) Immunoblotting of synaptic markers detected by anti-synaptophysin, synaptotagmin, PSD95, and β-actin antibodies in the Tris-soluble fraction of brain lysates from *MAPT*, *MAPT*$^{S305N;Int10+3;S320F}$, and *MAPT*$^{P301S;Int10+3;S320F}$ mice at 12 months of age (n = 4 per group, 2 males and 2 females).

(G) Gallyas silver staining in the HY of *MAPT*, *MAPT*$^{S305N;Int10+3;S320F}$, and *MAPT*$^{P301S;Int10+3;S320F}$ mice and in the AM of PS19 mice at 12 months of age as a positive control. Scale bars: 50 μm.

(legend continued on next page)

genotype differences were observed in the complete shifts (CSs)-only session, where two diagonal movement pattern shifts are repeated (Figure 6E, top). However, in the more complicated CSs/partial shifts (PSs)-shuffled session, which is composed of six movement pattern shifts, both mutant lines required significantly more trials to reach the criterion throughout the CS/PS phases compared to control mice (group effect, $F(2, 377) = 7.642$, $p < 0.001$; $p < 0.01$ for both mutant lines compared to control), indicating their difficulty in learning and behavioral flexibility in a task with higher cognitive load (Figure 6E, bottom). We observed no changes in the number of nosepokes per corner visit in the two tests, showing normal activity of mice (Figure S7B). See the STAR Methods for detailed experimental procedures.

Fourth, we assessed the ability of behavioral inhibition and sustained attention. In this test, mice had to withhold nosepokes for several seconds (delay time [DT]) while keeping attention on the light-emitting diode (LED) lights, a signal for a chance to acquire the water reward (Figure 6F). A nosepoke during the DT is recorded as a premature response, and the response time to the LED lights after the DT serves as an indicator of the degree of sustained attention. A total of four sessions were conducted, with the DT extended as the sessions progressed. *MAPT*$^{P301S;Int10+3;S320F}$ mice exhibited a longer response time compared to *MAPT* control mice in sessions 3 and 4, indicating impairment in sustained attention. A delay in response time also emerged in *MAPT*$^{S305N;Int10+3;S320F}$ mice when the DT was further extended in session 4 (Figures 6F and S7C). In addition, in *MAPT*$^{P301S;Int10+3;S320F}$, the percentages of "time-out" trials in which the nosepoke was not performed within the 5 s time limit in the task increased significantly. These results were a sign of decline in sustained attention.

Finally, to assess anhedonia and apathy-like behavior, we conducted the sweet taste preference test and the effort-based choice test using 0.1% saccharin water as a hedonic reward. There were no genotype differences in the sweet taste preference test, indicating that both mutant lines had the ability to perceive palatability (Figure 6G, left). On the other hand, in the effort-based choice test, both mutant lines exhibited a significantly lower preference for saccharin water compared to the control when incremental efforts (i.e., the number of nosepokes) were required to obtain the reward (group effect, $F(2, 261) = 14.50$, $p < 0.0001$; $p < 0.001$ for both mutant lines compared to control) (Figure 6G, right). This implied that the mutant lines had an apathy-like trait, specifically as elevated effort aversion.

In summary, *MAPT*$^{P301S;Int10+3;S320F}$ mice exhibited signs of elevated anxiety, repetitive behavior, impaired learning and behavioral flexibility, impaired sustained attention, and apathy-like behavior, partially overlapping with the clinical features of FTD (Figure 6H). A similar pattern of behavioral phenotypes was observed in the *MAPT*$^{S305N;Int10+3;S320F}$ mice, though to a lesser extent. We also observed a body weight increase in *MAPT*$^{P301S;Int10+3;S320F}$ mice, indicating increased food intake or abnormal metabolism (Figure S7D).

Effect of Aβ deposition on tau pathology in *MAPT*$^{P301S;Int10+3;S320F}$ mice

We crossbred *App*$^{NL-G-F}$ mice with *MAPT*$^{P301S;Int10+3;S320F}$ mice and obtained *App*$^{NL-G-F}$ × *MAPT*$^{P301S;Int10+3;S320F}$ mice to investigate whether *MAPT*$^{P301S;Int10+3;S320F}$ mice are applicable for studying β-amyloid (Aβ) and tau interactions. Intriguingly, AT8 positivity was markedly enhanced by the existence of amyloid plaques, particularly in the cortex and hippocampus (Figures 7A and 7B). However, the Aβ plaque density remained unchanged compared with *App*$^{NL-G-F}$ (Figures 7C and 7D), indicating that tau pathology did not influence Aβ plaque formation. Furthermore, GFAP and Iba1 immunosignals were not different between *App*$^{NL-G-F}$ and *App*$^{NL-G-F}$ × *MAPT*$^{P301S;Int10+3;S320F}$ (Figures 7E–7G), suggesting that neuroinflammation was triggered by Aβ plaques regardless of the presence of tau pathology. Taken together, Aβ plaques, or their process of formation, direct abnormal tau to the hippocampus and cortex and significantly accelerate tau pathology in those regions.

DISCUSSION

MAPT mutations are causes of FTDP-17 but not AD. Nevertheless, the exclusively Aβ deposition-dependent tau pathology exhibited by *MAPT*$^{P301S;Int10+3}$ mice crossbred with *App*$^{NL-G-F}$ mice[11] demonstrates an evident cause-and-effect relationship between Aβ and tau pathologies. This is consistent with previous observations showing that massive tau pathology takes place in the cortex/hippocampus after Aβ deposition in aging human brains[36–42] and that transgenic amyloid precursor protein (APP) or APP/PS1 overexpression accelerates tau pathology and neurodegeneration in mutant tau-transgenic mice.[43–49] In this way, the mutant *MAPT* KI mice described in the present study should be highly suitable for preclinical studies of both FTDP-17 and AD. Because hippocampal tau pathology in *App*$^{NL-G-F}$ mice crossbred with *MAPT*$^{P301S;Int10+3}$ mice takes almost 24 months,[11] we decided to analyze tau pathology in *App*$^{NL-G-F}$ mice crossbred with *MAPT*$^{P301S;Int10+3;S320F}$ mice. The presence of Aβ deposition caused a significant increase of tau pathology in this mutant mouse line, particularly in the hippocampus and cortex, from as early as 6 months of age. While more detailed analyses will be necessary, these bigenic mice will serve as a relevant model that reconstitutes the Aβ-tau axis observed in aging human brains.

In clear contrast to the *MAPT*$^{P301S;Int10+3;S320F}$ mice, the *MAPT*$^{P301S;Int10+3}$ mice that lack the S320F mutation exhibited minimal tau pathology up to 24 months of age,[11] indicating that the combination of P301S and S320F mutations affects

(H and I) Regional analysis of T1 MRI images obtained from *MAPT*, *MAPT*$^{S305N;Int10+3;S320F}$ and *MAPT*$^{P301S;Int10+3;S320F}$ mice at the age of 12 months ($n = 5$ per group, female). Scale bars: 1 mm.

In (B) and (E), the data are presented as the mean ± SD (one-way ANOVA with Tukey's multiple comparison test). *$p < 0.05$, **$p < 0.01$, ***$p < 0.005$. In (F) and (I), the data are presented as the mean ± SD (two-way ANOVA with Tukey's multiple comparison test). *$p < 0.05$, **$p < 0.01$, ***$p < 0.005$, ****$p < 0.001$. See also Figure S5 and S6.

CellPress
OPEN ACCESS

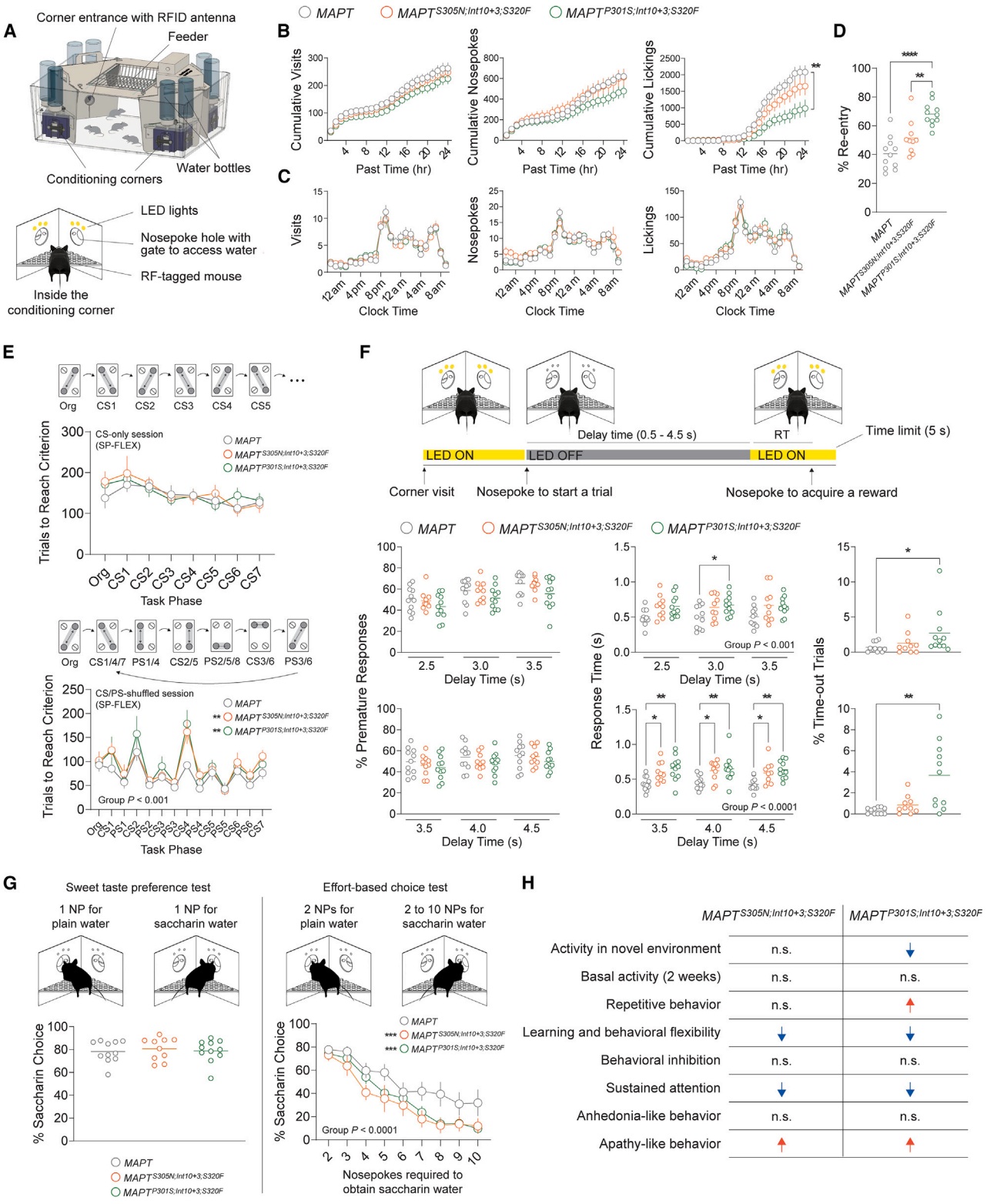

Figure 6. Behavioral abnormalities in triple-mutant *MAPT* KI mouse lines using the IntelliCage system

(A) Overview of the IntelliCage. Two IntelliCages were used to test a total of 32 female mice: *MAPT* (n = 11), *MAPT*$^{S305N;Int10+3;S320F}$ (n = 10), and *MAPT*$^{P301S;Int10+3;S320F}$ (n = 11); 5 or 6 mice per genotype per IntelliCage. The mice were assessed at ages ranging from 9 to 12 months, as this experiment lasted for 3 months.

(legend continued on next page)

the oligomeric status of tau protein in a synergistic manner. It would be helpful to determine the 3D structure of tau protein in these animals by cryoelectron microscopy,[50–54] as this may disclose how this particular combination of mutations affects the tau protein structure. Our findings are consistent with previous studies employing the combination of P301L/S and S320F mutations to show their synergistic effect on tau fibrillization using *in vitro*, transgenic, or adeno-associated virus-dependent paradigms.[14–16] We believe that one of the advantages of our KI models is stably reproducible *in vivo* phenotypes.

The mutant *MAPT* KI mice we generated will be useful for preclinical *in vivo* studies of FTDP-17, as they are not affected by overexpression artifact-related phenotypes. Because tau protein expression in the new models is driven by the endogenous murine *MAPT* promoter, it may be possible to observe tau pathology in non-neuronal cells, such as astrocytes,[55–58] although more detailed pathological investigations will be necessary. Thus far, we have been unable to histologically detect colocalization of pathological tau with GFAP.

Hyperphosphorylation of tau was detectable in $MAPT^{S305N;Int10+3}$ mice, accompanying synaptic loss and behavior abnormalities.[5] In contrast, both $MAPT^{P301S;Int10+3;S320F}$ and $MAPT^{S305N;Int10+3;S320F}$ mice, which fail to reproduce tau hyperphosphorylation, also displayed local brain atrophy and behavior abnormalities. These findings demonstrated that distinct pathways related to tau-mediated toxicity are likely involved in the early stages of the etiological events in tauopathies. Given that our model, $MAPT^{P301S;Int10+3;S320F}$, has TOC1-, T22-, and MC1-positive neurons and seed-competent high-order tau species with a physiological expression of tau driven by the *Mapt* promoter, rather than by overexpression, our data support a causal role of tau oligomers/fibrils in the pathomechanism(s) linked to neurotoxicity. However, the exact mechanisms by which tau oligomers/fibrils are associated with synaptic integrity, local brain atrophy, and behavior performance in these mutants require further investigation.

FTD primarily manifests through emotional blunting, lack of insight, repetitive stereotyped behaviors, and apathy.[59–61] In our current study, we employed the IntelliCage system, which indicated a notable score for re-entering the same corner (a sign of repetitive behavior) during the assessment of basal activities in $MAPT^{P301S;Int10+3;S320F}$ mice. Additionally, we identified deficits in sustained attention and aspects of apathy in the effort-based choice test on $MAPT^{P301S;Int10+3;S320F}$ mice, which is in agreement with previous studies.[62] These findings support the notion that $MAPT^{P301S;Int10+3;S320F}$ mice serve as a more appropriate animal model than conventional tau transgenic mice for recapitulating the clinical symptoms of FTD and testing the therapeutic strategies aimed at reducing toxic tau. Behavior differences reinforce the evidence of loss of viable synapses and neurodegeneration.

The partial success of lecanemab and donanemab, which target Aβ oligomers and pyroglutamyl Aβ, respectively, in clinical trials for treating early AD suggests that immunotherapies aimed at pathological tau may also be effective in treating FTDP-17, AD, and other tauopathies, although, to our knowledge, none of the clinical trials have yet succeeded. Experimental efforts to identify tau species that should be targeted will be required to facilitate the development of immunotherapies. We believe that the isogenic lines of mutant *MAPT* KI we generated will aid in providing a better understanding of which toxic tau species are targetable in different pathophysiological contexts and how to prevent disease progression by comparing them in a side-by-side manner.

Finally, there will be more uses of these mutant *MAPT* KI lines in terms of cell biology applications. Establishment of embryonic stem cells (ESCs) or induced pluripotent stem cells (iPSCs) from the mutant mice will also make it possible to strategically generate drug candidates by, for instance, using ESC- or iPSC-derived neurons or organoids for *in vitro* drug screening. It would also be fascinating to apply proteolysis-targeting chimera technology to reduce the tau pathology load.[63–67]

Limitations of the study

In the present study, we used a combination of triple mutations to generate our FTD models, which does not happen in the real world; i.e., in clinical human cases. In this respect, our model mice are artificial, but we believe that this is one of the best approaches to reproducing the pathological phenotypes without inducing overexpression artifacts. We would like to emphasize here that the genome editing technology is applicable only to KI animals because transgene(s) are generally inserted into multiple loci in a random manner in the overexpressing transgenic animals.[68]

(B) Activity in a novel environment. Hourly cumulative number of corner visits, nosepokes, and licking bouts during the first 24 h after the mice were introduced to the IntelliCage.

(C) Basal activity represented as daily averages over a 14-day period.

(D) Frequency of re-entries to the same corner in all patterns of corner-to-corner movements.

(E) Learning and behavioral flexibility assessment. Shown is the number of trials to reach criterion required for completing each phase of the CS-only session (top) and the CS/PS-shuffled session (bottom).

(F) Behavioral inhibition and sustained attention test. Mice were required to withhold nosepokes during the delay time (DT). Nosepokes during the DT were recorded as premature responses. The response time between the second LED-on signal and the subsequent nosepoke was used as a measure of sustained attention.

(G) Sweet taste preference test and effort-based choice test. In both tests, one side of the nosepoke hole in each corner led to saccharin water, while the other side led to plain water. For the sweet taste preference test, the percentage of saccharin choice over 2 days is plotted. For the effort-based choice test, the percentage of saccharin choice is plotted against the number of nosepokes required to obtain saccharin water.

(H) Summary of behavioral test results observed in mutant lines from the IntelliCage experiments.

The data are presented as the mean ± SD. Statistical significance was examined by two-way/one-way ANOVA (B–G) and Tukey's multiple comparisons test. $^{*}p < 0.05$, $^{**}p < 0.01$, $^{***}p < 0.005$, $^{****}p < 0.001$. See also Figure S7.

CellPress
OPEN ACCESS

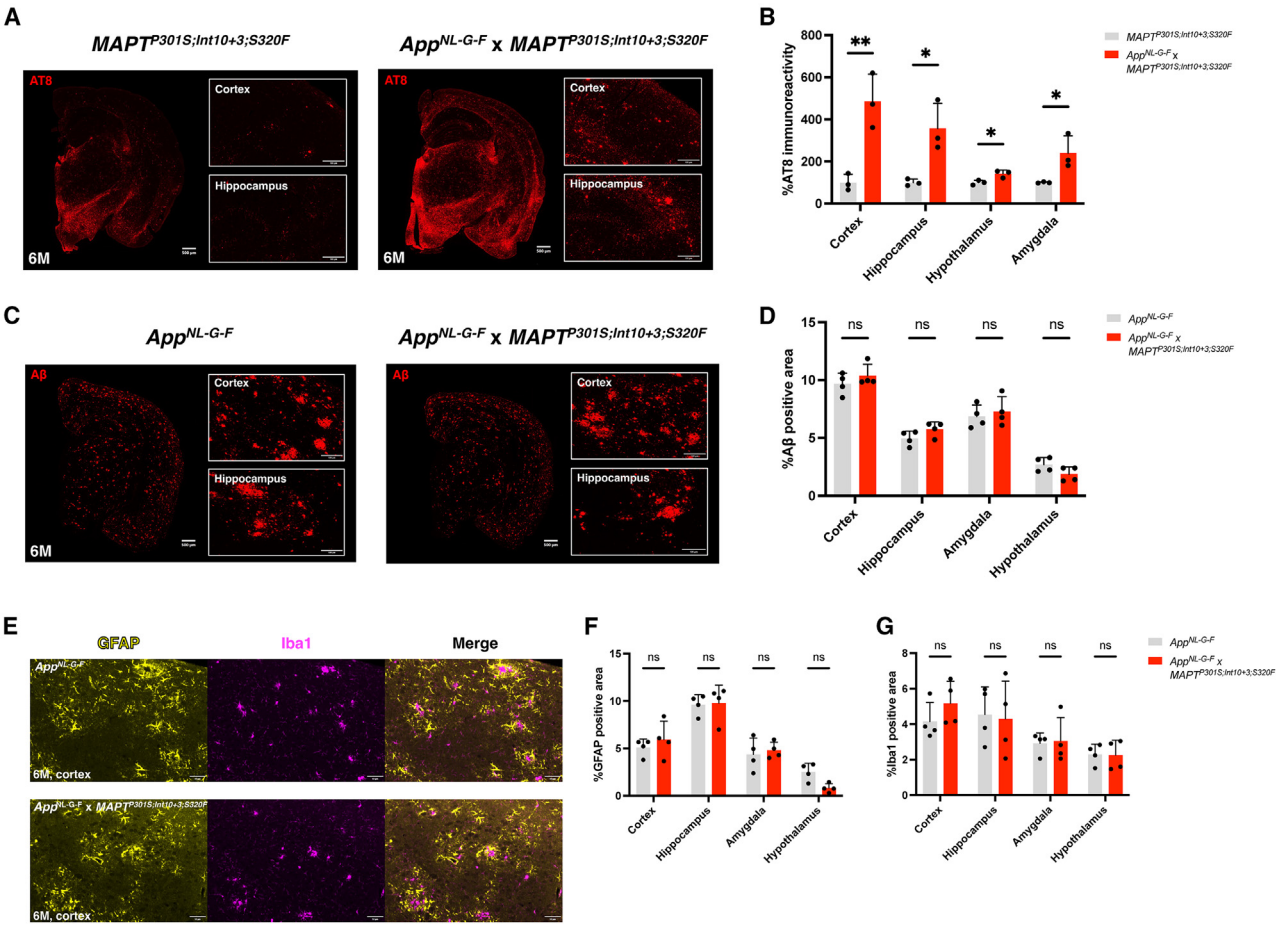

Figure 7. Effects of Aβ deposition on tau pathology in the hippocampus and cortex of *MAPT*$^{P301S;Int10+3;S320F}$ mice

(A and B) Representative AT8 immunostaining images of brain sections from *MAPT*$^{P301S;Int10+3;S320F}$ and *App*$^{NL-G-F}$ × *MAPT*$^{P301S;Int10+3;S320F}$ mice at the age of 6 months (A) and their quantification in cortex, hippocampus, HY, and AM regions (n = 3 per group, 2 males and 1 female) (B). Scale bars: 500 μm and 100 μm (insets).

(C and D) Representative Aβ immunostaining images of brain sections from *App*$^{NL-G-F}$ and *App*$^{NL-G-F}$ × *MAPT*$^{P301S;Int10+3;S320F}$ mice at the age of 6 months (C) and their quantification in cortex, hippocampus, HY, and AM regions (n = 4 per group, 2 males and 2 females) (D). Scale bars: 500 μm and 100 μm (insets).

(E–G) Immunostaining of GFAP and Iba1 in the brain sections from *App*$^{NL-G-F}$ and *App*$^{NL-G-F}$ × *MAPT*$^{P301S;Int10+3;S320F}$ mice at the age of 6 months (E) and regional quantification of positive area of GFAP (F) and Iba1 (G) (n = 4 per group, 2 males and 2 females).

In (B), the data are presented as the mean ± SD (two-way ANOVA with Tukey's multiple comparison test). $^{*}p < 0.05$, $^{**}p < 0.01$.

We did not examine the protein structure of tau fibrils carrying the P301S/S305N and S320F mutations. Further research is needed to determine whether the accumulated tau in these models replicates the pathological tau structure observed in FTD patients.

RESOURCE AVAILABILITY

Lead contact

Requests for information and resources should be directed to the lead contact, Takaomi Saido (takaomi.saido@riken.jp).

Materials availability

The datasets generated and/or analyzed during the current study are available from the corresponding authors upon reasonable request. All unique/stable reagents generated in this study, including mutant mouse lines (listed in Table S1), are available from the lead contact with a completed materials transfer agreement.

Data and code availability

- The whole-genome resequencing data are available from SRA (NCBI) with the accession number SAMN46105978 (*MAPT*$^{P301S;Int10+3;S320F}$), SAMN46105979 (*MAPT*$^{S305N;Int10+3;S320F}$), and SAMN46105980 (*MAPT*$^{S305N;Int10+3;S320Y}$) under project accession number PRJNA1152251.
- This paper does not report original code.
- Any additional information required to reanalyze the data reported in this work paper is available from the lead contact upon request.

ACKNOWLEDGMENTS

We thank Ryo Fujioka and Naoko Mihira at RIKEN CBS and Shoko Uchida and Akira Sumiyoshi at QST for technical advice. We also express our gratitude to Yukiko Nagai-Watanabe for her secretarial assistance. This work was supported by a RIKEN Aging Project grant, Strategic Research Program for Brain Sciences and the Japan Agency for Medical Research and Development grant JP20dm0207001, JSPS KAKENHI grant

23K26790 (to T.C.S.), JSPS KAKENHI grant 21K15378, JSPS Overseas Research Fellowships, the RIKEN FY2020 Incentive Research Project, The Uehara Memorial Foundation Research Fellowship, The Cell Science Research Foundation Research Fellowship, Alzheimer's Association Research Fellowship (to N.W.), and JSPS KAKENHI grant 24K18633 (to T.M.). Work undertaken at the UK Dementia Research Institute, University College London, was supported by the UK Dementia Research Institute, through UK DRI Ltd., principally funded by the Medical Research Council.

AUTHOR CONTRIBUTIONS

Conceptualization, T.M., M.Q., T.C.S., and N.W.; methodology, T.M., M.Q., H.S., S. Benner, T.E., H.H., H.M., and N.W.; investigation, T.M., M.Q., N.K., S. Bez, M.F., T.E., S. Benner, H.M., and N.W.; visualization, T.M., M.Q., T.E., H.K., and H.M.; funding acquisition, T.C.S. and N.W.; project administration, T.C.S. and N.W.; supervision, K.D., A.M., M.S., M.H., T.C.S., and N.W.; writing – original draft, T.M., M.Q., T.C.S., and N.W.; writing – review & editing, H.S., S.B., M.F., K.D., S.B., T.E., H.H., H.K., A.M., H.M., N.S., M.S., and M.H.

DECLARATION OF INTERESTS

The RIKEN IP Office has filed patents for the triple mutant *MAPT* KI mouse lines with N.W., T.M., N.K., M.Q., H.S., and T.C.S. as inventors. T.C.S. serves as a consultant for RIKEN BIO Co. Ltd.

STAR★METHODS

Detailed methods are provided in the online version of this paper and include the following:

- KEY RESOURCES TABLE
- EXPERIMENTAL MODEL AND STUDY PARTICIPANT DETAILS
  - Animals
  - Cell culture and growth conditions
- METHOD DETAILS
  - Brain samples preparation
  - RNA extraction and semi-quantitative RT-PCR
  - Western blot analysis after alkaline phosphatase treatment
  - Sarkosyl fractionation
  - Western blot
  - Immunohistochemistry
  - DAB staining
  - Transduction of biosensor cell lines, flow cytometry, and seeding analysis
  - Flow cytometry
  - Gallyas silver staining
  - MRI
  - Generation of triple mutant *MAPT* KI mouse lines
  - Whole genome resequencing
  - Behavior analyses using the IntelliCage
  - Behavioral inhibition and sustained attention test
  - Sweet taste preference and effort-based choice test
- QUANTIFICATION AND STATISTICAL ANALYSIS

SUPPLEMENTAL INFORMATION

Supplemental information can be found online at https://doi.org/10.1016/j.crmeth.2025.101024.

Received: August 14, 2024
Revised: February 26, 2025
Accepted: March 19, 2025
Published: April 11, 2025

REFERENCES

1. Wang, Y., and Mandelkow, E. (2016). Tau in physiology and pathology. Nat. Rev. Neurosci. *17*, 22–35. https://doi.org/10.1038/nrn.2015.1.
2. Hashimoto, S., Matsuba, Y., Kamano, N., Mihira, N., Sahara, N., Takano, J., Muramatsu, S.I., Saido, T.C., and Saito, T. (2019). Tau binding protein CAPON induces tau aggregation and neurodegeneration. Nat. Commun. *10*, 2394. https://doi.org/10.1038/s41467-019-10278-x.
3. Saito, T., Mihira, N., Matsuba, Y., Sasaguri, H., Hashimoto, S., Narasimhan, S., Zhang, B., Murayama, S., Higuchi, M., Lee, V.M.Y., et al. (2019). Humanization of the entire murine Mapt gene provides a murine model of pathological human tau propagation. J. Biol. Chem. *294*, 12754–12765. https://doi.org/10.1074/jbc.RA119.009487.
4. Komor, A.C., Kim, Y.B., Packer, M.S., Zuris, J.A., and Liu, D.R. (2016). Programmable editing of a target base in genomic DNA without double-stranded DNA cleavage. Nature *533*, 420–424. https://doi.org/10.1038/nature17946.
5. Watamura, N., Foiani, M., Bez, S., Bourdenx, M., Santambrogio, A., Frodsham, C., Camporesi, E., Brinkmalm, G., Zetterberg, H., Patel, S., et al. (2024). In vivo hyperphosphorylation of tau is associated with synaptic loss and behavioral abnormalities in the absence of tau seeds. Nat. Neurosci., 1–15. *in press*.
6. Saito, T., Matsuba, Y., Mihira, N., Takano, J., Nilsson, P., Itohara, S., Iwata, N., and Saido, T.C. (2014). Single App knock-in mouse models of Alzheimer's disease. Nat. Neurosci. *17*, 661–663. https://doi.org/10.1038/nn.3697.
7. Saito, T., Matsuba, Y., Yamazaki, N., Hashimoto, S., and Saido, T.C. (2016). Calpain Activation in Alzheimer's Model Mice Is an Artifact of APP and Presenilin Overexpression. J. Neurosci. *36*, 9933–9936. https://doi.org/10.1523/jneurosci.1907-16.2016.
8. Hashimoto, S., Ishii, A., Kamano, N., Watamura, N., Saito, T., Ohshima, T., Yokosuka, M., and Saido, T.C. (2018). Endoplasmic reticulum stress responses in mouse models of Alzheimer's disease: Overexpression paradigm versus knockin paradigm. J. Biol. Chem. *293*, 3118–3125. https://doi.org/10.1074/jbc.M117.811315.
9. Sasaguri, H., Nilsson, P., Hashimoto, S., Nagata, K., Saito, T., De Strooper, B., Hardy, J., Vassar, R., Winblad, B., and Saido, T.C. (2017). APP mouse models for Alzheimer's disease preclinical studies. EMBO J. *36*, 2473–2487. https://doi.org/10.15252/embj.201797397.
10. Sasaguri, H., Hashimoto, S., Watamura, N., Sato, K., Takamura, R., Nagata, K., Tsubuki, S., Ohshima, T., Yoshiki, A., Sato, K., et al. (2022). Recent Advances in the Modeling of Alzheimer's Disease. Front. Neurosci. *16*, 807473. https://doi.org/10.3389/fnins.2022.807473.
11. Saido, T.C. (2024). Alzheimer's Disease Research Guide: Animal Models for Understanding Mechanisms and Medications (Elsevier Inc).
12. Hashimoto, S., and Saido, T.C. (2018). Critical review: involvement of endoplasmic reticulum stress in the aetiology of Alzheimer's disease. Open Biol. *8*, 180024. https://doi.org/10.1098/rsob.180024.
13. Gamache, J., Benzow, K., Forster, C., Kemper, L., Hlynialuk, C., Furrow, E., Ashe, K.H., and Koob, M.D. (2019). Factors other than hTau overexpression that contribute to tauopathy-like phenotype in rTg4510 mice. Nat. Commun. *10*, 2479. https://doi.org/10.1038/s41467-019-10428-1.
14. Koller, E.J., Gonzalez De La Cruz, E., Machula, T., Ibanez, K.R., Lin, W.L., Williams, T., Riffe, C.J., Ryu, D., Strang, K.H., Liu, X., et al. (2019). Combining P301L and S320F tau variants produces a novel accelerated model of tauopathy. Hum. Mol. Genet. *28*, 3255–3269. https://doi.org/10.1093/hmg/ddz151.
15. Strang, K.H., Croft, C.L., Sorrentino, Z.A., Chakrabarty, P., Golde, T.E., and Giasson, B.I. (2018). Distinct differences in prion-like seeding and aggregation between Tau protein variants provide mechanistic insights into tauopathies. J. Biol. Chem. *293*, 2408–2421. https://doi.org/10.1074/jbc.M117.815357.

16. Xia, Y., Prokop, S., Bell, B.M., Gorion, K.M.M., Croft, C.L., Nasif, L., Xu, G., Riffe, C.J., Manaois, A.N., Strang, K.H., et al. (2022). Pathogenic tau recruits wild-type tau into brain inclusions and induces gut degeneration in transgenic SPAM mice. Commun. Biol. *5*, 446. https://doi.org/10.1038/s42003-022-03373-1.

17. Chen, D., Bali, S., Singh, R., Wosztyl, A., Mullapudi, V., Vaquer-Alicea, J., Jayan, P., Melhem, S., Seelaar, H., van Swieten, J.C., et al. (2023). FTD-tau S320F mutation stabilizes local structure and allosterically promotes amyloid motif-dependent aggregation. Nat. Commun. *14*, 1625. https://doi.org/10.1038/s41467-023-37274-6.

18. Cradick, T.J., Qiu, P., Lee, C.M., Fine, E.J., and Bao, G. (2014). COSMID: A Web-based Tool for Identifying and Validating CRISPR/Cas Off-target Sites. Mol. Ther. Nucleic Acids *3*, e214. https://doi.org/10.1038/mtna.2014.64.

19. Blaudin de Thé, F.X., Lassus, B., Schaler, A.W., Fowler, S.L., Goulbourne, C.N., Jeggo, R., Mannoury la Cour, C., Millan, M.J., and Duff, K.E. (2021). P62 accumulates through neuroanatomical circuits in response to tauopathy propagation. acta neuropathol. commun. *9*, 177. https://doi.org/10.1186/s40478-021-01280-w.

20. d'Abramo, C., Acker, C.M., Jimenez, H.T., and Davies, P. (2013). Tau passive immunotherapy in mutant P301L mice: antibody affinity versus specificity. PLoS One *8*, e62402. https://doi.org/10.1371/journal.pone.0062402.

21. Jeganathan, S., Hascher, A., Chinnathambi, S., Biernat, J., Mandelkow, E.M., and Mandelkow, E. (2008). Proline-directed pseudo-phosphorylation at AT8 and PHF1 epitopes induces a compaction of the paperclip folding of Tau and generates a pathological (MC-1) conformation. J. Biol. Chem. *283*, 32066–32076. https://doi.org/10.1074/jbc.M805300200.

22. Jicha, G.A., Bowser, R., Kazam, I.G., and Davies, P. (1997). Alz-50 and MC-1, a new monoclonal antibody raised to paired helical filaments, recognize conformational epitopes on recombinant tau. J. Neurosci. Res. *48*, 128–132. https://doi.org/10.1002/(sici)1097-4547(19970415)48:2<128::aid-jnr5>3.0.co;2-e.

23. Vitale, F., Giliberto, L., Ruiz, S., Steslow, K., Marambaud, P., and d'Abramo, C. (2018). Anti-tau conformational scFv MC1 antibody efficiently reduces pathological tau species in adult JNPL3 mice. Acta Neuropathol. Commun. *6*, 82. https://doi.org/10.1186/s40478-018-0585-2.

24. Sahara, N., and Kimura, T. (2018). Biochemical Properties of Pathology-Related Tau Species in Tauopathy Brains: An Extraction Protocol for Tau Oligomers and Aggregates. Methods Mol. Biol. *1779*, 435–445. https://doi.org/10.1007/978-1-4939-7816-8_26.

25. Furman, J.L., and Diamond, M.I. (2017). FRET and Flow Cytometry Assays to Measure Proteopathic Seeding Activity in Biological Samples. Methods Mol. Biol. *1523*, 349–359. https://doi.org/10.1007/978-1-4939-6598-4_23.

26. Holmes, B.B., Furman, J.L., Mahan, T.E., Yamasaki, T.R., Mirbaha, H., Eades, W.C., Belaygorod, L., Cairns, N.J., Holtzman, D.M., and Diamond, M.I. (2014). Proteopathic tau seeding predicts tauopathy in vivo. Proc. Natl. Acad. Sci. USA *111*, E4376–E4385. https://doi.org/10.1073/pnas.1411649111.

27. Yoshiyama, Y., Higuchi, M., Zhang, B., Huang, S.M., Iwata, N., Saido, T.C., Maeda, J., Suhara, T., Trojanowski, J.Q., and Lee, V.M.Y. (2007). Synapse loss and microglial activation precede tangles in a P301S tauopathy mouse model. Neuron *53*, 337–351. https://doi.org/10.1016/j.neuron.2007.01.010.

28. Spires-Jones, T.L., and Hyman, B.T. (2014). The intersection of amyloid beta and tau at synapses in Alzheimer's disease. Neuron *82*, 756–771. https://doi.org/10.1016/j.neuron.2014.05.004.

29. Rexach, J.E., Polioudakis, D., Yin, A., Swarup, V., Chang, T.S., Nguyen, T., Sarkar, A., Chen, L., Huang, J., Lin, L.C., et al. (2020). Tau Pathology Drives Dementia Risk-Associated Gene Networks toward Chronic Inflammatory States and Immunosuppression. Cell Rep. *33*, 108398. https://doi.org/10.1016/j.celrep.2020.108398.

30. Voikar, V., Colacicco, G., Gruber, O., Vannoni, E., Lipp, H.P., and Wolfer, D.P. (2010). Conditioned response suppression in the IntelliCage: assessment of mouse strain differences and effects of hippocampal and striatal lesions on acquisition and retention of memory. Behav. Brain Res. *213*, 304–312. https://doi.org/10.1016/j.bbr.2010.05.019.

31. Krackow, S., Vannoni, E., Codita, A., Mohammed, A.H., Cirulli, F., Branchi, I., Alleva, E., Reichelt, A., Willuweit, A., Voikar, V., et al. (2010). Consistent behavioral phenotype differences between inbred mouse strains in the IntelliCage. Gene Brain Behav. *9*, 722–731. https://doi.org/10.1111/j.1601-183X.2010.00606.x.

32. Masuda, A., Kobayashi, Y., Kogo, N., Saito, T., Saido, T.C., and Itohara, S. (2016). Cognitive deficits in single App knock-in mouse models. Neurobiol. Learn. Mem. *135*, 73–82. https://doi.org/10.1016/j.nlm.2016.07.001.

33. Lipp, H.P., Krackow, S., Turkes, E., Benner, S., Endo, T., and Russig, H. (2024). IntelliCage: the development and perspectives of a mouse- and user-friendly automated behavioral test system. Front. Behav. Neurosci. *17*, 1270538. https://doi.org/10.3389/fnbeh.2023.1270538.

34. Seelaar, H., Kamphorst, W., Rosso, S.M., Azmani, A., Masdjedi, R., de Koning, I., Maat-Kievit, J.A., Anar, B., Donker Kaat, L., Breedveld, G.J., et al. (2008). Distinct genetic forms of frontotemporal dementia. Neurology *71*, 1220–1226. https://doi.org/10.1212/01.wnl.0000319702.37497.72.

35. Balan, S., Iwayama, Y., Ohnishi, T., Fukuda, M., Shirai, A., Yamada, A., Weirich, S., Schuhmacher, M.K., Dileep, K.V., Endo, T., et al. (2021). A loss-of-function variant in SUV39H2 identified in autism-spectrum disorder causes altered H3K9 trimethylation and dysregulation of protocadherin β-cluster genes in the developing brain. Mol. Psychiatr. *26*, 7550–7559. https://doi.org/10.1038/s41380-021-01199-7.

36. Thal, D.R., Rüb, U., Orantes, M., and Braak, H. (2002). Phases of A beta-deposition in the human brain and its relevance for the development of AD. Neurology *58*, 1791–1800. https://doi.org/10.1212/wnl.58.12.1791.

37. Knopman, D.S., Parisi, J.E., Salviati, A., Floriach-Robert, M., Boeve, B.F., Ivnik, R.J., Smith, G.E., Dickson, D.W., Johnson, K.A., Petersen, L.E., et al. (2003). Neuropathology of cognitively normal elderly. J. Neuropathol. Exp. Neurol. *62*, 1087–1095. https://doi.org/10.1093/jnen/62.11.1087.

38. Braak, H., Alafuzoff, I., Arzberger, T., Kretzschmar, H., and Del Tredici, K. (2006). Staging of Alzheimer disease-associated neurofibrillary pathology using paraffin sections and immunocytochemistry. Acta Neuropathol. *112*, 389–404. https://doi.org/10.1007/s00401-006-0127-z.

39. Nelson, P.T., Braak, H., and Markesbery, W.R. (2009). Neuropathology and Cognitive Impairment in Alzheimer Disease: A Complex but Coherent Relationship. J. Neuropathol. Exp. Neurol. *68*, 1–14. https://doi.org/10.1097/NEN.0b013e3181919a48.

40. Braak, H., Thal, D.R., Ghebremedhin, E., and Del Tredici, K. (2011). Stages of the Pathologic Process in Alzheimer Disease: Age Categories From 1 to 100 Years. J. Neuropathol. Exp. Neurol. *70*, 960–969. https://doi.org/10.1097/NEN.0b013e318232a379.

41. Davidson, Y.S., Robinson, A., Prasher, V.P., and Mann, D.M.A. (2018). The age of onset and evolution of Braak tangle stage and Thal amyloid pathology of Alzheimer's disease in individuals with Down syndrome. Acta Neuropathol. Commun. *6*, 56. https://doi.org/10.1186/s40478-018-0559-4.

42. Robinson, A.C., Davidson, Y.S., Horan, M.A., Pendleton, N., and Mann, D.M.A. (2018). Pathological Correlates of Cognitive Impairment in The University of Manchester Longitudinal Study of Cognition in Normal Healthy Old Age. J. Alzheimers Dis. *64*, 483–496. https://doi.org/10.3233/jad-180171.

43. Gomes, L.A., Hipp, S.A., Rijal Upadhaya, A., Balakrishnan, K., Ospitalieri, S., Koper, M.J., Largo-Barrientos, P., Uytterhoeven, V., Reichwald, J., Rabe, S., et al. (2019). Aβ-induced acceleration of Alzheimer-related τ-pathology spreading and its association with prion protein. Acta Neuropathol. *138*, 913–941. https://doi.org/10.1007/s00401-019-02053-5.

44. Ribé, E.M., Pérez, M., Puig, B., Gich, I., Lim, F., Cuadrado, M., Sesma, T., Catena, S., Sánchez, B., Nieto, M., et al. (2005). Accelerated amyloid deposition, neurofibrillary degeneration and neuronal loss in double mutant APP/tau transgenic mice. Neurobiol. Dis. *20*, 814–822. https://doi.org/10.1016/j.nbd.2005.05.027.

45. Arner, A., Rockenstein, E., Mante, M., Florio, J., Masliah, D., Salehi, B., Adame, A., Overk, C., Masliah, E., and Rissman, R.A. (2018). Increased Vulnerability of the Hippocampus in Transgenic Mice Overexpressing APP and Triple Repeat Tau. J Alzheimers Dis *61*, 1201–1219. https://doi.org/10.3233/jad-170388.

46. Bolmont, T., Clavaguera, F., Meyer-Luehmann, M., Herzig, M.C., Radde, R., Staufenbiel, M., Lewis, J., Hutton, M., Tolnay, M., and Jucker, M. (2007). Induction of tau pathology by intracerebral infusion of amyloid-beta -containing brain extract and by amyloid-beta deposition in APP x Tau transgenic mice. Am. J. Pathol. *171*, 2012–2020. https://doi.org/10.2353/ajpath.2007.070403.

47. Lewis, J., Dickson, D.W., Lin, W.L., Chisholm, L., Corral, A., Jones, G., Yen, S.H., Sahara, N., Skipper, L., Yager, D., et al. (2001). Enhanced neurofibrillary degeneration in transgenic mice expressing mutant tau and APP. Science *293*, 1487–1491. https://doi.org/10.1126/science.1058189.

48. Pérez, M., Morán, M.A., Ferrer, I., Ávila, J., and Gómez-Ramos, P. (2008). Phosphorylated tau in neuritic plaques of APP(sw)/Tau (vlw) transgenic mice and Alzheimer disease. Acta Neuropathol. *116*, 409–418. https://doi.org/10.1007/s00401-008-0420-0.

49. Pérez, M., Ribe, E., Rubio, A., Lim, F., Morán, M.A., Ramos, P.G., Ferrer, I., Isla, M.t.g., and Avila, J. (2005). Characterization of a double (amyloid precursor protein-tau) transgenic: tau phosphorylation and aggregation. Neuroscience *130*, 339–347. https://doi.org/10.1016/j.neuroscience.2004.09.029.

50. Fitzpatrick, A.W.P., Falcon, B., He, S., Murzin, A.G., Murshudov, G., Garringer, H.J., Crowther, R.A., Ghetti, B., Goedert, M., and Scheres, S.H.W. (2017). Cryo-EM structures of tau filaments from Alzheimer's disease. Nature *547*, 185–190. https://doi.org/10.1038/nature23002.

51. Scheres, S.H., Zhang, W., Falcon, B., and Goedert, M. (2020). Cryo-EM structures of tau filaments. Curr. Opin. Struct. Biol. *64*, 17–25. https://doi.org/10.1016/j.sbi.2020.05.011.

52. Scheres, S.H.W., Ryskeldi-Falcon, B., and Goedert, M. (2023). Molecular pathology of neurodegenerative diseases by cryo-EM of amyloids. Nature *621*, 701–710. https://doi.org/10.1038/s41586-023-06437-2.

53. Schweighauser, M., Murzin, A.G., Macdonald, J., Lavenir, I., Crowther, R.A., Scheres, S.H.W., and Goedert, M. (2023). Cryo-EM structures of tau filaments from the brains of mice transgenic for human mutant P301S Tau. acta neuropathol. commun. *11*, 160. https://doi.org/10.1186/s40478-023-01658-y.

54. Tarutani, A., Lövestam, S., Zhang, X., Kotecha, A., Robinson, A.C., Mann, D.M.A., Saito, Y., Murayama, S., Tomita, T., Goedert, M., et al. (2023). Cryo-EM structures of tau filaments from SH-SY5Y cells seeded with brain extracts from cases of Alzheimer's disease and corticobasal degeneration. FEBS Open Bio *13*, 1394–1404. https://doi.org/10.1002/2211-5463.13657.

55. Wang, X., Yang, H., Liu, C., and Liu, K. (2023). A new diagnostic tool for brain disorders: extracellular vesicles derived from neuron, astrocyte, and oligodendrocyte. Front. Mol. Neurosci. *16*, 1194210. https://doi.org/10.3389/fnmol.2023.1194210.

56. Wang, Y.T.T., Rosa-Neto, P., and Gauthier, S. (2023). Advanced brain imaging for the diagnosis of Alzheimer disease. Curr. Opin. Neurol. *36*, 481–490. https://doi.org/10.1097/wco.0000000000001198.

57. Edison, P. (2024). Astroglial activation: Current concepts and future directions. Alzheimers Dement *20*, 3034–3053. https://doi.org/10.1002/alz.13678.

58. He, L., Duan, X., Li, S., Zhang, R., Dai, X., and Lu, M. (2024). Unveiling the role of astrocytes in postoperative cognitive dysfunction. Ageing Res. Rev. *95*, 102223. https://doi.org/10.1016/j.arr.2024.102223.

59. Neary, D., Snowden, J., and Mann, D. (2005). Frontotemporal dementia. Lancet Neurol. *4*, 771–780. https://doi.org/10.1016/s1474-4422(05)70223-4.

60. Zhu, C.W., Grossman, H.T., and Sano, M. (2022). Apathy and Functional Impairment in the Course of Behavioral Variant Frontotemporal Dementia. JAMA Netw. Open *5*, e2245656. https://doi.org/10.1001/jamanetworkopen.2022.45656.

61. Le Bouc, R., Borderies, N., Carle, G., Robriquet, C., Vinckier, F., Daunizeau, J., Azuar, C., Levy, R., and Pessiglione, M. (2023). Effort avoidance as a core mechanism of apathy in frontotemporal dementia. Brain *146*, 712–726. https://doi.org/10.1093/brain/awac427.

62. Robinson, L., Dreesen, E., Mondesir, M., Harrington, C., Wischik, C., and Riedel, G. (2024). Apathy-like behaviour in tau mouse models of Alzheimer's disease and frontotemporal dementia. Behav. Brain Res. *456*, 114707. https://doi.org/10.1016/j.bbr.2023.114707.

63. Jangampalli Adi, P., and Reddy, P.H. (2021). Phosphorylated tau targeted small-molecule PROTACs for the treatment of Alzheimer's disease and tauopathies. Biochim. Biophys. Acta, Mol. Basis Dis. *1867*, 166162. https://doi.org/10.1016/j.bbadis.2021.166162.

64. Kargbo, R.B. (2019). Treatment of Alzheimer's by PROTAC-Tau Protein Degradation. ACS Med. Chem. Lett. *10*, 699–700. https://doi.org/10.1021/acsmedchemlett.9b00083.

65. Liu, Z., Hu, M., Yang, Y., Du, C., Zhou, H., Liu, C., Chen, Y., Fan, L., Ma, H., Gong, Y., and Xie, Y. (2022). An overview of PROTACs: a promising drug discovery paradigm. Mol. Biomed. *3*, 46. https://doi.org/10.1186/s43556-022-00112-0.

66. Tashima, T. (2023). Proteolysis-Targeting Chimera (PROTAC) Delivery into the Brain across the Blood-Brain Barrier. Antibodies *12*, 43. https://doi.org/10.3390/antib12030043.

67. Wang, W., Zhou, Q., Jiang, T., Li, S., Ye, J., Zheng, J., Wang, X., Liu, Y., Deng, M., Ke, D., et al. (2021). A novel small-molecule PROTAC selectively promotes tau clearance to improve cognitive functions in Alzheimer-like models. Theranostics *11*, 5279–5295. https://doi.org/10.7150/thno.55680.

68. Tosh, J.L., Rickman, M., Rhymes, E., Norona, F.E., Clayton, E., Mucke, L., Isaacs, A.M., Fisher, E.M.C., and Wiseman, F.K. (2017). The integration site of the APP transgene in the J20 mouse model of Alzheimer's disease. Wellcome Open Res. *2*, 84. https://doi.org/10.12688/wellcomeopenres.12237.1.

69. Furman, J.L., Holmes, B.B., and Diamond, M.I. (2015). Sensitive Detection of Proteopathic Seeding Activity with FRET Flow Cytometry. J. Vis. Exp. https://doi.org/10.3791/53205.

70. Hiramoto, T., Sumiyoshi, A., Kato, R., Yamauchi, T., Takano, T., Kang, G., Esparza, M., Matsumura, B., Stevens, L.J., Hiroi, Y.J., et al. (2024). Highly demarcated structural alterations in the brain and impaired social incentive learning in Tbx1 heterozygous mice. Mol. Psychiatr., 1. https://doi.org/10.1038/s41380-024-02797-x.

71. Ma, Y., Smith, D., Hof, P.R., Foerster, B., Hamilton, S., Blackband, S.J., Yu, M., and Benveniste, H. (2008). Vivo 3D Digital Atlas Database of the Adult C57BL/6J Mouse Brain by Magnetic Resonance Microscopy. Front. Neuroanat. *2*, 1. https://doi.org/10.3389/neuro.05.001.2008.

72. Sasaguri, H., Nagata, K., Sekiguchi, M., Fujioka, R., Matsuba, Y., Hashimoto, S., Sato, K., Kurup, D., Yokota, T., and Saido, T.C. (2018). Introduction of pathogenic mutations into the mouse Psen1 gene by Base Editor and Target-AID. Nat. Commun. *9*, 2892. https://doi.org/10.1038/s41467-018-05262-w.

73. Hsu, P.D., Scott, D.A., Weinstein, J.A., Ran, F.A., Konermann, S., Agarwala, V., Li, Y., Fine, E.J., Wu, X., Shalem, O., et al. (2013). DNA targeting specificity of RNA-guided Cas9 nucleases. Nat. Biotechnol. *31*, 827–832. https://doi.org/10.1038/nbt.2647.

74. Raczy, C., Petrovski, R., Saunders, C.T., Chorny, I., Kruglyak, S., Margulies, E.H., Chuang, H.Y., Källberg, M., Kumar, S.A., Liao, A., et al. (2013). Isaac: ultra-fast whole-genome secondary analysis on Illumina sequencing platforms. Bioinformatics *29*, 2041–2043. https://doi.org/10.1093/bioinformatics/btt314.

75. Cingolani, P., Platts, A., Wang, L.L., Coon, M., Nguyen, T., Wang, L., Land, S.J., Lu, X., and Ruden, D.M. (2012). A program for annotating and predicting the effects of single nucleotide polymorphisms, SnpEff: SNPs in the genome of Drosophila melanogaster strain w1118. Fly (Austin) *6*, 80–92. https://doi.org/10.4161/fly.19695 iso-2; iso-3. .

76. Kiryk, A., Janusz, A., Zglinicki, B., Turkes, E., Knapska, E., Konopka, W., Lipp, H.P., and Kaczmarek, L. (2020). IntelliCage as a tool for measuring mouse behavior - 20 years perspective. Behav. Brain Res. *388*, 112620. https://doi.org/10.1016/j.bbr.2020.112620.

77. Hurst, J.L., and West, R.S. (2010). Taming anxiety in laboratory mice. Nat. Methods *7*, 825–826. https://doi.org/10.1038/nmeth.1500.

78. Endo, T., Maekawa, F., Võikar, V., Haijima, A., Uemura, Y., Zhang, Y., Miyazaki, W., Suyama, S., Shimazaki, K., Wolfer, D.P., et al. (2011). Automated test of behavioral flexibility in mice using a behavioral sequencing task in IntelliCage. Behav. Brain Res. *221*, 172–181. https://doi.org/10.1016/j.bbr.2011.02.037.

STAR★METHODS

KEY RESOURCES TABLE

REAGENT or RESOURCE	SOURCE	IDENTIFIER
Antibodies		
CP13	Kindly provided by Peter Davies	RRID:AB_2314223
AT8	Thermo Fisher Scientific	Cat# MN1020; RRID:AB_223647
PHF1	Kindly provided by Peter Davies	RRID:AB_2315150
TOC1	Novus	Cat# NBP3-20163; RRID:AB_3608371
T22	Sigma-Aldrich	Cat# ABN454; RRID:AB_2888681
MC1	Kindly provided by Peter Davies	RRID:AB_2314773
Tau13	Santa Cruz Biotechnology	Cat# sc-21796; RRID:AB_628328
Tau5	Thermo Fisher Scientific	Cat# AHB0042; RRID:AB_2536235
MAP2	Abcum	Cat# ab183830; RRID:AB_2895301
KIF5A	Proteintech	Cat# 21186-1-AP; RRID:AB_10733125
GA5 (Anti-GFAP)	Merck Millipore	Cat# MAB360; RRID:AB_11212597
Anti-Iba1	Fujifilm-wako	Cat# 013–27691; RRID:AB_2934095
Synaptotagmin	Synaptic System	Cat# 105-002; RRID:AB_887830
Homer1	Synaptic System	Cat# 160-004; RRID:AB_2619855
Synaptophysin	PROGEN	Cat# 61012
PSD-95	Synaptic System	Cat# 124-011; RRID:AB_2619799
N1D (Anti-Aβ)	In-house (Saido et al. 1994)	N/A
Anti-β-actin, HRP	Proteintech	Cat# HRP-60008; RRID:AB_2819183
Anti-Rabbit IgG, HRP	Proteintech	Cat# SA00001-2; RRID:AB_2722564
Anti-Mouse IgG, HRP	Proteintech	Cat# SA00001-1; RRID:AB_2722565
Chemicals, peptides, and recombinant proteins		
4% paraformaldehyde	Nacalai Tesque	Cat# 09154-85
RNAiso Plus	Takara Bio	Cat# 9109
ReverTra Ace	TOYOBO	Cat# FSQ-301
cOmplete protease inhibitor cocktail	Roche Diagnostics	Cat# 11697498001
lambda-phosphatase	Santa Cruz Biotechnology	Cat# sc-200312A
ECL prime blocking buffer	GE healthcare	Cat# RPN418
ECL Select detection reagent	GE Healthcare	Cat# RPN2235
Tris-EDTA buffer (pH 8.0) (TE buffer)	Nacalai Tesque	Cat# 06890-54
0.5% blocking reagent powder	AKOYA Biosciences	Cat# SKU FP1012
VECTASTAIN Elite ABC-HRP Kit	Vector Laboratories	Cat# PK-6100
DMEM	Thermo Fisher Scientific	Cat# 41966-029
Lipofectamine 2000	Invitrogen	Cat# 11668019
Opti-MEM	Gibco	Cat# 31985070
Herculase II Fusion DNA Polymerase	Agilent Technologies	Cat# 600675
mMESSAGE mMACHINE T7 Ultra Transcription kit	Thermo Fisher Scientific	Cat# AM1345
MEGAshortscript T7	Thermo Fisher Scientific	Cat# AM1354
MEGAclear	Thermo Fisher Scientific	Cat# AM1908
Ex Taq-Polymerase kit	Takara Bio	Cat# RR001A
PhosSTOP	Roche Diagnostics	Cat# 12352204
ProLong Gold Antifade Mountant	Invitrogen	Cat# P36934

(*Continued on next page*)

Continued

REAGENT or RESOURCE	SOURCE	IDENTIFIER
Deposited data		
Whole genome resequencing data (MAPTP301S; Int10 + 3; S320F)	This paper	SAMN46105978
Whole genome resequencing data (MAPTS305N; Int10 + 3; S320F)	This paper	SAMN46105979
Whole genome resequencing data (MAPTS305N; Int10 + 3; S320Y)	This paper	SAMN46105980
Experimental models: Cell lines		
HEK Tau RD P301S FRET biosensors	ATCC	Cat# CRL-3275,RRID:CVCL_DA04
Experimental models: Organisms/strains		
B6.Cg-Mapt<em(MAPT/P301S; S320F; Intron10 + 3 G>A)Tcs>	RIKEN BRC	RBRC11768
B6.Cg-Mapt<em(MAPT/S305N; S320F; Intron10 + 3 G>A)Tcs>	RIKEN BRC	RBRC11769
B6.Cg-Mapt<em(MAPT/S305N; S320Y; Intron10 + 3 G>A)Tcs>	RIKEN BRC	RBRC11770
Oligonucleotides		
3R-Tau F (RT-PCR)	Eurofin Genetics	GTCCGTACTCCACCCAAGTC
3R-Tau R (RT-PCR)	Eurofin Genetics	TTTGTAGACTATTTGCACCTTCC
4R-Tau F (RT-PCR)	Eurofin Genetics	GAAGCTGGATCTTAGCAACG
4R-Tau R (RT-PCR)	Eurofin Genetics	GACGTGTTTGATATTATCCT
Total Tau F (RT-PCR)	Eurofin Genetics	AGCCAAGACATCCACACGTT
Total Tau R (RT-PCR)	Eurofin Genetics	ATCAGAGGGTCTGAGCTACCA
G3PDH F (RT-PCR)	Eurofin Genetics	CCATGGCACCGTCAAGGCTGA
G3PDH R (RT-PCR)	Eurofin Genetics	GCCAGTAGAGGCAGGGATGAT
BE F	Eurofin Genetics	GCCGCTAATACGACTCACTATAG
BE R	Eurofin Genetics	GCCGCTAATACGACTCACTATAG
sgRNA F	Eurofin Genetics	TAATACGACTCACTATAGGCTCCAAG TGTGGCTCATTGTTTTAGAGCTAGAA
sgRNA R	Eurofin Genetics	AAAAGCACCGACTCGGTGCCACTTTT TCAAGTTGATAACGGACTAGCCTTATTT TAACTTGCTATTTCTAGCTCTAAAAC
Human MAPT F (common) (Genotyping)	Eurofin Genetics	GTCAGATCACTAGACTCAGC
Human MAPT R1 (WT) (Genotyping)	Eurofin Genetics	CTGTGCTCCACTGTGACTGG
Human MAPT R2 (MT) (Genotyping)	Eurofin Genetics	CTGCTTGAGTTATCTTGGCC
Humanized mouse App E16WT(Genotyping)	Eurofin Genetics	ATCTCGGAAGTGAAGATG
Humanized mouse App E16MT (Genotyping)	Eurofin Genetics	ATCTCGGAAGTGAATCTA
Humanized mouse App WT (Genotyping)	Eurofin Genetics	TGTAGATGAGAACTTAAC
Humanized mouse App *loxP* (Genotyping)	Eurofin Genetics	CGTATAATGTATGCTATACGAAG
PS19 (Tau-Tg_P301S) F(common) (Genotyping)	Eurofin Genetics	TTGAAGTTGGGTTATCAATTTGG
PS19 (Tau-Tg_P301S) R1 (WT) (Genotyping)	Eurofin Genetics	TTCTTGGAACACAAACCATTTC
PS19 (Tau-Tg_P301S) R2 (MT) (Genotyping)	Eurofin Genetics	AAATTCCTCAGCAACTGTGGT
Human MAPT_repeat identifier 3R/4R ratio F	Eurofin Genetics	AAGTCGCCGTCTTCCGCCAAG
Human MAPT_repeat identifier 3R/4R ratio R	Eurofin Genetics	GTCCAGGGACCCAATCTTCGA

(*Continued on next page*)

Continued

REAGENT or RESOURCE	SOURCE	IDENTIFIER
human MAPT exon10 301 Seq F	Eurofin Genetics	CTCATCGAAAGTGGAGGCGT
human MAPT exon10 301 Seq R	Eurofin Genetics	GGTCCGTCATCTGCCCTATT
human MAPT exon11 332 Seq F	Eurofin Genetics	GCTTACACAGCTGCTTCTCA
human MAPT exon11 332 Seq R	Eurofin Genetics	TTTCACTTCACTCCCGCCTC
App_Ex16_NL_Seq Seq F	Eurofin Genetics	ACAGGCATTACATATTCAGCGT
App_Ex16_NL_Seq Seq R	Eurofin Genetics	ACTATCAACAGAGCCCCACT
App_Ex17_GF_Seq Seq F	Eurofin Genetics	TGTGCCCTGAGTACCACAGA
App_Ex17_GF_Seq Seq R	Eurofin Genetics	TGCTCATTGTTCCAGAGACG
Recombinant DNA		
pCMV-BE3	Addgene plasmid	Cat# 73021; RRID:Addgene_73021
Software and algorithms		
Image Lab (ver. 6.1.0)	Biorad	https://www.bio-rad.com/en-jp/product/image-lab-software?ID=KRE6P5E8Z
GraphPad Prism 10 (ver. 10.4.1)	GraphPad	https://www.graphpad.com/
bioRender	bioRender	https://www.biorender.com/
SnapGene (ver. 8.0.1)	Dotmatics	https://www.snapgene.com/

EXPERIMENTAL MODEL AND STUDY PARTICIPANT DETAILS

Animals

All animal experiments were conducted in accordance with the guidelines of the RIKEN Center for Brain Science and UK Animal Act, 1968, and following local ethical advice. All experiments follow the ARRIVE guidelines. C57BL/6J and ICR mice were used as zygote donors and foster mothers. C57BL/6J mice were also used for backcrossing of mutant *MAPT* KI mice. *MAPT* KI mice were generated as previously described.[2,3] *MAPT* $^{P301S;\ Int10+3}$ and *MAPT* $^{S305N;\ Int10+3}$ KI mice were also obtained as described.[5] In this study, mouse samples were collected from four individuals (primarily two males and two females) at 6, 9, and 12 months of age. The details were also indicated in each figure legend.

Cell culture and growth conditions

HEK Tau RD P301S FRET biosensors (ATCC CRL-3275) were cultured in DMEM (Thermofisher #41966-029) supplemented with 10% FBS and 1% Penicillin-Streptomycin (Gibco, 15140122) for seeding assays.

METHOD DETAILS

Brain samples preparation

Mice were perfused with PBS for 2 min after anesthesia. The brain was collected and sectioned along the midline to separate the two hemispheres. One side was immediately cut into five samples (cortex 1, 2, 3 from anterior to posterior, hippocampus, thalamus), frozen in liquid nitrogen, and stored at −80°C. The other side was incubated in 4% paraformaldehyde (Nacalai Tesque #09154-85) overnight at 4°C, washed in PBS, and embedded in paraffin for sectioning.

RNA extraction and semi-quantitative RT-PCR

Total RNA was extracted from mouse brain cortices using RNAiso Plus (Takara #9109) according to the manufacturer's instructions. Reverse transcription was performed using ReverTra Ace (TOYOBO FSQ-301). Semi-quantitative real-time PCR was conducted using the QuantStudio system (Thermo Fisher Scientific). Primer pairs are listed as described.[5]

Western blot analysis after alkaline phosphatase treatment

Mouse brains were homogenized in lysis buffer (50 mM Tris pH 7.6, 0.15 M NaCl, cOmplete protease inhibitor cocktail (Roche Diagnostics #11697498001)) using a Multi-bead shocker MB (Yasui-Kikai). Samples were rotated at 4°C for 1 h and centrifuged at 19800xg for 30 min. Supernatants were collected as lysates and then subjected to sodium dodecyl sulfate-polyacrylamide gel electrophoresis (SDS-PAGE), followed by transfer to a PVDF membrane. For detection of the tau isoform pattern, brain lysates were dephosphorylated with lambda-phosphatase (Santa Cruz Biotechnology #sc-200312A) according to the manufacturer's protocols. Membranes were then treated with ECL prime blocking buffer (GE healthcare RPN418) for 1 h and incubated with antibody at 4°C. Dilution ratios of antibodies are 1:2000 (Tau13) and 1:30000 (β-actin, HRP). Immunoreactive bands were visualized with ECL

Select detection reagent (GE Healthcare RPN2235) and a LAS-3000 Mini Lumino image analyzer (Fujifilm). Image Lab (Biorad) was used for the data analysis.

Sarkosyl fractionation

Sarkosyl fractionation was performed as described previously.[24] Briefly, frozen brain tissues were weighed and homogenized in homogenization buffer (TBS supplemented with protease inhibitor and phosphatase inhibitor cocktail) with 0.1 g tissue weight/ml concentration, followed by ultracentrifugation (26,300 x g, 4°C, 20 min). The supernatant was used as the S1 fraction (TBS-soluble fraction). The pellet was dissolved in high salt/sucrose buffer (10 mM Tris-HCl pH 7.5, 0.8 M NaCl, 10% sucrose, 1 mM EGTA, protease inhibitor, phosphatase inhibitor) with a half volume of homogenization buffer, followed by ultracentrifugation (26,300 x g, 4°C, 20 min). Sarkosyl solution was added to the obtained supernatant for a 1% concentration, and the solution was incubated at 37°C for 1 h. Finally, the P3 fraction (sarkosyl-insoluble fraction) was obtained by ultracentrifugation (150,000 x g, 4°C, 1 h). P3 was dissolved in 0.5 μL/mg brain tissue Tris-EDTA buffer (pH 8.0) (TE buffer) (06890-54, Nacalai tesque) for western blot analysis.

Western blot

S1 and P3 fractions were subjected to SDS-PAGE, followed by transfer to a PVDF membrane. The protein concentration of S1 fraction was measured by BCA assay to adjust the concentration. Membranes were then treated with ECL prime blocking buffer (GE healthcare RPN418) for 1 h and incubated with antibody at 4°C. Dilution ratios of antibodies are 1:1000 (CP13), 1:1000 (AT8), 1:1000 (PHF-1), 1:2000 or 1:5000 (Tau13), 1:1000 (Tau5), 1:1000 (Synaptotagmin), 1:2000 (Synaptophysin), 1:1000 (PSD-95), 1:30000 (Anti-β-actin, HRP), 1:5000 (Anti-Rabbit IgG, HRP) and 1:5000 (Anti-Mouse IgG, HRP). Immunoreactive bands were visualized with ECL Select detection reagent (GE Healthcare RPN2235) and a LAS-3000 Mini Lumino image analyzer (Fujifilm).

Immunohistochemistry

Paraffin-embedded mouse brain sections were deparaffinized and applied to antigen retrieval by autoclaving sections at 121°C for 5 min in 0.01 M citrate buffer (pH 6.0). Sections were then rinsed in tap water, treated with 0.3% H_2O_2 in methanol to inactivate endogenous peroxidases, rinsed in water and TNT buffer (0.1M Tris-HCl pH 7.5, 0.15M NaCl, 0.05% Triton X-100), and blocked in blocking solution composed of 0.5% blocking reagent powder (AKOYA Biosciences, SKU FP1012) in TNB buffer (0.1M Tris-HCl pH 7.5, 0.15M NaCl). The sections were incubated overnight at 4°C with primary antibodies diluted by TNB buffer and washed three times in TNT for 5 min, followed by incubation in biotinylated secondary antibodies diluted by TNB buffer at room temperature for 1 h. Dilution ratios of primary/secondary antibodies are 1:3000 (CP13), 1:200 (AT8), 1:500 (PHF-1), 1:1000 (TOC-1), 1:200 (T22), 1:200 (MC1), 1:8000 (MAP2), 1:100 (KIF5A), 1:200 (Anti-Iba1), 1:500 (Aynaptotagmin), 1:500 (Homer1) and 1:200 (N1D). After washing three times for 5 min, the sections were incubated in horseradish peroxidase (HRP)-conjugated streptavidin for 30 min, washed in TNT, and applied to tyramide-fluorescein isothiocyanate or tyramide-rhodamine solution for 10 min. Finally, the sections were stained with DAPI (Cell Signaling Technology #4083S) diluted in TNB buffer before mounting with ProLong Gold Antifade Mountant (Invitrogen, P36934). The mounted sections were scanned with a VS200 digital slide scanner (Evident) for tau pathology and Andor BC43 spinning disk confocal for axon and dendrite observations. For the generation of heat maps in Figure 2C, scores ranging from 0 to 100 were derived through visual assessment alongside annotated anatomical brain regions on the atlas. The score data were imported into Prism for further analyses and procedures. Labels for the schematic images were added manually.

Super-resolution synapse images were obtained using a Zeiss LSM980 microscope with Airyscan detector with a 63x, 1.4-NA oil immersion Plan-Apochromat object. The images were processed in Zen Black using 3D Airyscan Processing. Imaris software was then used for pre-synaptic and post-synaptic *puncta* detection, using intensity centers to maximise the detection of immunoreactivity spots. Pre-synaptic and post-synaptic spots were colocalized using a MATLAB colocalization script (Colocalize Spots XTension), using a colocalization distance of 0.25 μm between spot centers. Dilution ratios of pre- and post-synaptic antibodies are 1:500 (synaptotagmin) and 1:500 (Homer1).

DAB staining

Paraffin-embedded mouse brain sections were deparaffinized and applied to antigen retrieval by autoclaving sections at 121°C for 5 min in 0.01 M citrate buffer (pH 6.0). Sections were then rinsed in tap water, treated with 0.3% H_2O_2 in methanol to inactivate endogenous peroxidases, rinsed in water. The following procedures were performed using VECTASTAIN Elite ABC-HRP Kit (Vector Laboratories, PK-6100) according to the provided protocol. The antibodies used and the concentration are the same as the above immunohistochemistry section.

Transduction of biosensor cell lines, flow cytometry, and seeding analysis

HEK Tau RD P301S FRET biosensors (ATCC CRL-3275) were cultured in DMEM (Thermofisher #41966-029) supplemented with 10% FBS and 1% Pen-Strep. The cells were plated at a density of 38,000 cells per well in a 96-well plate using a media volume of 130 μL per well. Eighteen hours later, the cells were transduced with proteopathic seeds. A mixture of 1.25 μL of Lipofectamine 2000 (Invitrogen) and 8.75 μL of Opti-MEM (Gibco, Life Technologies) was incubated at room temperature for 5 min before being combined with 10 μg of total protein (S1) and 1μL (P3) from mouse samples. Negative controls received Lipofectamine mixed with

Opti-MEM. Following a 30-min incubation at 37°C, a final volume of 20 μL was added to each well, and the cells were incubated for 48 h. Each sample included three technical replicates.

Flow cytometry

Tau RD P301S FRET biosensor cells were harvested using 0.25% trypsin and fixed in 4% PFA for 10 min, then resuspended in flow cytometry buffer (1X PBS and 1mM EDTA). An LSR Fortessa Flow Cytometer (BD Biosciences) was employed to conduct FRET flow cytometry on the Tau RD P301S FRET biosensors. FRET was quantified as previously described.[69] Briefly, single cells that were double-positive for YFP and CFP were identified, and FRET-positive cells within this population were quantified. The percentage of FRET (the number of FRET-positive cells divided by the total cell count) was used as an output measure. Data analysis was performed using FCS Express v7 (*De Novo* Software) and GraphPad Prism v9.4.1 for Mac OS X.

Gallyas silver staining

The sections were deparaffinized and hydrated with xylene and ethanol, then placed in 5% Periodic Acid for 3–5 min. Afterward, the sections were rinsed with water and placed in Silver Iodide solution (300mL of water containing 12g of Sodium Hydroxide, 30g of Potassium Iodide, and 10.5mL of 1% Silver Nitrate) for 1 min. They were then placed in 0.5% Acetic Acid for 10 min and rinsed with water. The sections were immersed in a solution containing 200mL of 5% anhydrous sodium carbonate, 100 mL of buffer (0.19g of ammonium nitrate, 0.2g of silver nitrate, 1g of Tungstosilicic Acid in water), and another 100mL of buffer (0.19g of ammonium nitrate, 0.2g of silver nitrate, 1g of Tungstosilicic Acid, and 0.76mL of 37% Formaldehyde in water), before development was stopped in 0.5% acetic acid for 5 min, followed by dehydration with ethanol and xylene.

MRI

MR images were acquired using a 7.0-T BioSpec 70/40 system with a ^{1}H receive-only 4-channel phased array MRI CryoProbe (Bruker, Billerica, MA, USA) with the software for operation (ParaVision 360 Ver. 3.4; Bruker). T1-weigheted anatomical brain images were obtained 3D Modified Driven Equilibrium Fourier Transform (MDEFT) sequence with the following parameters; repetition time 3000 ms, echo repetition time = 10 ms, echo time = 2.0 ms, inversion delay = 1100 ms, field of view = 18 × 18 × 18 mm^3, matrix size = 144 × 144 × 80 mm^3, voxel size = 0.125 × 0.125 × 0.125 mm^3, fat suppression = on, and number of average = 1. The scanning time was approximately 9 min for each mouse under inhalation anesthesia with 1.5% isoflurane. The acquired data were reconstructed and exported to the images using ParaVision software in DICOM format. Images were obtained by manually skull-stripping using PMOD software (ver. 4.1, PMOD Technologies LLC, Fällanden, Switzerland) to create the brain mask. The regional brain volume was measured utilizing a software package, the Advanced Normalization Tools following a published method[70] The anatomical image was non-linearly registered to the mouse MR atlas.[71]

Generation of triple mutant *MAPT* KI mouse lines

Preparation of BE mRNA and sgRNAs

Base Editor (BE) which is a fusion protein composed of *Streptococcus pyrogenes* Cas9 (SpCas9) and rat APOBEC1 (apolipoprotein B mRNA-editing enzyme, catalytic polypepide-like1)[4] was used for the introduction of the FTD-associated mutation (S320F) into the *MAPT* gene of *MAPT* $^{P301S;\ Int10+3}$ and *MAPT*$^{S305N;\ Int10+3}$ KI mice. For the synthesis of BE mRNA *in vitro*, plasmid vector pCMV-BE3 (Addgene plasmid #73021) was obtained from Addgene. To prepare the mRNA template for BE, PCR was performed with Herculase II Fusion DNA Polymerase (Agilent Technologies #600675). BE was then synthesized with the mMESSAGE mMACHINE T7 Ultra Transcription kit (Thermo Fisher Scientific #AM1345). The template for the *in vitro* transcription of sgRNA was also synthesized by PCR with Herculase II Fusion DNA Polymerase as previously described.[72] The MEGAshortscript T7 (Thermo Fisher Scientific #AM1354) and MEGAclear (Thermo Fisher Scientific #AM1908) kits were used for the *in vitro* transcription of sgRNA, while the CRISPR Design tool was used for creating sgRNA.[73] Oligonucleotide sequences used for the *in vitro* transcription of BE and sgRNA are described below.

BE: Forward 5′-GCCGCTAATACGACTCACTATAG-3′, Reverse 5′-GCCGCTAATACGACTCACTATAG-3′.

sgRNA: Forward 5′-TAATACGACTCACTATAGGCTCCAAGTGTGGCTCATTGTTTTAGAGCTAGAA-3′, Reverse 5′- AAAAGCACCGACTCGGTGCCACTTTTTCAAGTTGATAACGGACTAGCCTTATTTTAACTTGCTATTTCTAGCTCTAAAAC-3′.

Microinjection of mouse zygotes

BE mRNA (60 ng/μL) and sgRNA (200 ng/μL) were injected into the cytoplasm of *MAPT* $^{P301S;\ Int10+3}$ and *MAPT*$^{S305N;\ Int10+3}$ KI mice zygotes. After incubation at 37°C for 24 h, embryos developed to the 2-cell stage were transplanted into host ICR mice.

Off-target analysis

Off-target sites that accepted up to three mismatches were determined by COSMID (https://crispr.bme.gatech.edu/).[18] Target sites were amplified from tail genomic DNA by PCR using the Ex Taq-Polymerase kit (Takara #RR001A). Target sequencing was performed using a DNA sequencer (ABI 3730xl).

Whole genome resequencing

Library construction

DNA samples extracted from mouse tail were prepared according to the Illumina TruSeq DNA sample preparation guide to obtain a final library of 300-400bp average insert size. 100 ng of genomic DNA were fragmented by the Covaris system with specific tubes,

which generates double-strand DNA fragments with 3′ or 5′ overhangs. Fragmented DNAs were then converted into blunt ends using an End Repair Mix. The 3′ to 5′ exonuclease removes the 3′ overhangs, and the polymerase fills in the 5′ overhangs. Following the end repair, the appropriate library size was selected using different ratios of sample purification beads. Adenylation of 3′ ends was performed to prevent ligation during the adapter ligation reaction. A corresponding single "T" nucleotide on the 3′ end of the adapter provides a complementary overhang for ligating the adapter to the fragment. Multiple indexing adapters were ligated to the ends of the DNA fragments to prepare them for hybridizing onto a flow cell. PCR was used to amplify the enriched DNA library for sequencing. The PCR was performed with a PCR primer solution that annealed to the ends of each adapter.

Clustering and sequencing

For cluster generation, the library was loaded into a flow cell where fragments were captured on a lawn of surface-bound oligonucleotides complementary to the library adapters. Each fragment was then amplified into distinct clonal clusters through bridge amplification. When cluster generation was complete, the templates were ready for sequencing. Illumina SBS technology utilizes a proprietary reversible terminator-based method that detects single bases as they are incorporated into DNA template strands. As all four reversible, terminator-bound dNTPs were present during each sequencing cycle, natural competition minimized incorporation bias and greatly reduced raw error rates compared to other technologies. The result was a highly accurate, base-by-base sequencing that virtually eliminated sequence-context-specific errors, even within repetitive sequence regions and homopolymers.

Generation of raw data

The Illumina platform generates raw images and base calling through an integrated primary analysis software called Real-Time Analysis (RTA). The BCL (base calls) binary files were converted into FASTQ files using the Illumina package bcl2fastq2-v2.20.0.

Sequencing analysis

Resulting reads were aligned using Isaac Genome Alignment software (version 01.15.02.08), which is designed to align next-generation sequencing data with low-error rates,[74] and Isaac Variant Caller (IVC) (version 2.0.13), which is used for identifying single-nucleotide variants (SNVs) and small insertions and deletions in the diploid genome case. The annotation tool SnpEff was used to categorize the effect of variants on genes.[75]

Behavior analyses using the IntelliCage

Housing and testing environment

All behavior tests using IntelliCage (TSE Systems GmbH) were conducted at the animal facility of Phenovance LLC (Chiba, Japan) in accordance with that company's Animal Care and Use Committee guidelines (Experiment Approval Number: PRT202405_52RS). The animal facility was maintained at 20°C–26°C, 40–70% relative humidity, 10–25 ventilation per hour, and a 12 h light-dark cycle (8:00 ON, 20:00 OFF). Two weeks before starting the IntelliCage experiments, mice were anesthetized by isoflurane inhalation with the aid of an SN-487-1T Scan instrument (SHINANO manufacturing) and implanted with a small, glass-covered radio-frequency identification (RFID) tag via a disposable injector with needle (2.12 × 12 mm, FDX-B ISO11784/11785, FAREAD Technology). The mice were housed in conventional plastic cages (2000P type, 612 × 435 × 216 mm, Tecniplast) in groups of 12–13 animals until the experiment.

IntelliCage System

IntelliCage is a fully automated testing apparatus for monitoring spontaneous and cognitive behaviors of group-housed RFID-tagged mice in a home cage.[76] The corners of the cage are equipped with four triangular operant chambers (hereafter referred as corner A, B, C, and D) that permit the entry of a single mouse at a time. The RFID antenna at each corner entrance recognizes the tag ID implanted in each mouse, while infrared sensors and licking sensors inside the corner chambers monitor mouse behavior. Each corner holds two water bottles, the nozzles of which can be accessed through two nosepoke holes with motorized doors; the infrared beam-break response detector on the nosepoke hole responds to the mouse nosepokes which trigger door opening/closing. A small concrete block was placed in front of each corner as a footstool to make it easier for mice to enter the corner. Experimenters can flexibly program the rules for opening/closing of the doors and the lighting pattern of three LED lights located above each nosepoke hole. Two IntelliCages were used for experiments and each group of mice was divided as evenly as possible (5–6 mice per genotype per IntelliCage) for a total of 16 mice per IntelliCage. Each IntelliCage was usually cleaned once a week, at which time the general health of each mouse was also carefully checked (body weights were measured; condition of skin, hair, eyes, mouth, tail and basic walking movements in an open cage were visually assessed. During the experiment, each IntelliCage was placed in a soundproof wooden isolation box (Phenovance LLC) for environmental control.

Programs used for IntelliCage experiments

For the following IntelliCage experiments, each task program was selected from the Phenovance Task Library, which contains a collection of task programs for IntelliCage created by Phenovance LLC using specialized software (Designer software, TSE Systems).

Exploratory behavior, basal activity, repetitive/stereotypical behaviors

On the first day of the IntelliCage experiment, mice were transferred from the conventional 2000P cages to IntelliCages by "tunnel handling",[77] 2 h into the light period (10:00 a.m.). All doors in the corner chambers were kept open and mice were free to drink water from any corner. The number of corner visits, nosepokes, and lickings during the day were measured as indices of exploratory behaviors in novel environment. In the following 14 days, all the doors were closed and a single nosepoke opened the door for 3000 ms to allow mice to drink water. The number of corner visits, nosepokes, and lickings from the 14 days were used to calculate the indices of basal activity level and repeptitive/stereotypical behaviors (corner visiting patterns, corner preferences, side preferences).

Self-paced learning and behavioral flexibility test (SP-FLEX)

This test is designed to assess the learning ability of mice to the behavioral sequence rule and behavioral flexibility to adapt to repetitive rule shifts (modified from an original protocol developed in a previous study).[78] Each mouse was assigned a pair of corners as rewarding corners and had to shuttle between them to obtain water as a reward; water could not be obtained from the other two corners (non-rewarding corners) until the rule switched. When a mouse nosepoked at one of the rewarding corners, the door opened for 2000 ms to permit the water intake, with the following restrictions: 1) The door opened only once per visit, and 2) a mouse was not permitted to obtain the reward by consecutively re-entering the same corner. Because of these restrictions, mice were forced to go back and forth between the assigned two rewarding corners in order to obtain the reward, one defined as the active corner and the other as the inactive corner. A success response was defined as obtaining a reward by a direct move from the previously active rewarding corner to the current active rewarding corner, while a failure response was defined as visiting one of the two non-rewarding corners and applying at least one nosepoke. The success and failure responses were automatically detected and input to Wald's sequential probability ratio test (SPRT) statistics to calculate each mouse's probability of success. The significance level for the acceptance of each criterion was 0.05. Corner visits without nosepokes were omitted from the SPRT calculation. Whenever the performance of a mouse reached the pre-set upper criterion (30%), the assignment of rewarding and non-rewarding corners for that mouse switched. Note that the switch only occurred for mice whose success rate reached the upper criterion of SPRT. The test consisted of two sessions called the "CS (complete shift)-only" session and the "CS (complete shift)/PS (partial shift)-shuffled" session, each of which lasted 24 h per day for ten days. The detailed protocol for each session is described below (see also a previous study conducted using the same protocol).[35]

Session 1. CS (complete shift)-only session: In this session, the mice were required to learn a behavioral sequence in which they were rewarded for moving back and forth between two diagonally opposite corners (e.g., corners A, C) out of four corners (corners A, B, C, D). When the performance reached the upper criterion of SPRT, the two corners that had been rewarding (corners A and C) and the two non-rewarding corners (corners B and D) were reversed. Note that the term "complete shift" or "CS" means that all the previously rewarding corners and all the previously non-rewarding corners were reversed at the same time. Within a session, there were multiple test phases: The Original learning phase (Org) is the phase of initial learning of the behavioral sequence rule until the first reversal occurs; Org was followed by the CS1 phase, when the rewarding and non-rewarding corner assignments reversed for the first time; the phases proceed every time the reversal occurs (e.g., CS2, CS3, and so on).

Session 2. CS (complete shift)/PS (partial shift)-shuffled session: In this session, the same protocol as in the CS-only session was used until the end of the CS1 phase. When a mouse reached the upper criterion of SPRT in the CS1 phase, only one of the two rewarding corners was replaced by one of the two non-rewarding corners (henceforth referred to as "partial shift" or "PS"). After that, the CS and PS phases were alternately imposed on each mouse. All combinations of the two corners out of four corners were presented twice each.

The number of trials, which is defined as the sum of the success and failure responses required to reach the upper criterion, was used to assess the efficiency of learning and behavioral flexibility at each task phase. In addition, the average numbers of nosepokes per active rewarding corner, inactive rewarding corner, and non-rewarding corners were calculated as secondary indices of behavioral flexibility. This is based on the notion that no matter what type of corner visit it is, more than a single nosepoke is redundant in this task: The second nosepoke will not provide any further reward in the active rewarding corner, and neither the inactive rewarding corner nor the non-rewarding corner provide reward, regardless of how many nosepoke attempts a mouse may make. Therefore, repetitive nosepokes in each corner visit can be interpreted as an inability to flexibly terminate the meaningless actions; in other words, behavioral inflexibility derived from impulsive or perseverative characteristics.

Behavioral inhibition and sustained attention test

This test was designed based on the protocol of an operant schedule called differential reinforcement of low rates with limited hold (DRL-LH): the protocol assesses whether mice could maintain impulsive nosepoking behavior under control for a certain amount of time and whether they could sustain attention during that time.

In this test, all mice were permitted to obtain water as a reward in any of the four corners by making nosepokes in a way that followed the rules below: When a mouse entered a corner, the leftmost and rightmost LED lights above nosepoke holes were lit yellow. The LED lights turned off when the mouse made its first nosepoke on either side, but the door did not open. Then, after a certain amount of time (delay time; DT), the LED lights turned back on (reward signal), at which time the mouse could obtain a reward by making its second nosepoke. The door opened for 4000 ms in response to the nosepoke; after it closed, the trial for that corner visit ended, meaning that the mouse had to leave the corner and re-enter it for more reward.

On the first day of the training phase (Training Day 1), the delay time was set to 0, so mice were rewarded for nosepoking twice in a row. On Training Day 2, the delay time was set to 100 ms, on Training Day 3–200 ms, and on Training Days 4–5 to 500 ms. If the mouse nosepoked during the delay time, the timer was set back to zero, meaning that mice had to suppress nosepoke activity during the delay time in order to obtain rewards in an efficient manner.

At the end of Training Day 5, the following four test sessions were conducted (four days per session): In Session 1, a delay time of 500 ms, 1000 ms, or 1500 ms was presented randomly in each trial. If a nosepoke was made during the delay time, the timer was set

back to zero and recorded as one premature response. In the analysis, the percent of premature responses during each delay time was used as an indicator of the difficulty of behavioral inhibitory control. A nosepoke during the reward signal opened the door for 4000 ms to permit mice to drink water as a reward. However, the reward signals were presented only for 5 s, and if no nosepoke was made during that time, the reward opportunity was lost for that trial. The response time between the presentation of the reward signal and the nosepoke was used as a measure of sustained attention. In Session 2, random DTs of 1000 ms, 1500 ms, or 2000 ms were applied. In Session 3, random delays of 1500 ms, 2000 ms, or 2500 ms were applied. In Session 4, random delays of 2500 ms, 3000 ms, or 3500 ms were applied. Otherwise, the rules were the same as in Session 1. For each of Sessions 1, 2, 3 and 4, data from the second day onward were used to evaluate performance, as the first day of each four-day session required familiarization with the new delay time condition.

Sweet taste preference and effort-based choice test

0.1% saccharin (199–08665, FUJIFILM Wako Pure Chemical Corporation) water was used as the hedonic reward, preferred by the C57BL/6 strain.

In the sweet taste preference test and the subsequent effort-based choice test, mice were able to freely drink saccharin or plain water from any of the four corners; in two corners, they were able to drink saccharin water from the right nosepoke holes and plain water from the left. In the remaining two corners, the positions of the left and right bottles were reversed.

The protocol for the sweet taste preference test was as follows. When a mouse visited a corner, the doors of the left and right nosepoke holes were automatically opened. When the mouse nosepoked on either side, the door on the side of the nosepoke closed after 1500 ms (henceforth called the ‘‘tasting trial’’). After the tasting trial, when the mouse nosepoked the closed door again, the door opened for 2000 ms (hereafter called ‘‘preference-based choice’’). The mouse could repeat the preference-based choice as many times as it wanted in a single corner visit. In the analysis, the percentage of preference-based choices made for saccharin water out of the total choices made for both types of solutions was used as a sweet taste preference index. The test was conducted over two days. Day 1 began at 12:00 noon, 4 h after the start of the light period, with the saccharin and plain water bottles inserted into the IntelliCage. On the second day of the test, the positions of the bottles on the left and right sides of each corner were reversed at 12:00 noon. The mean value of the preference-based choice rate for the saccharin water on each day was used as a representative value for comparison between groups. After confirming that no significant difference in preference for the 0.1% saccharin water was apparent between the groups, the degree of motivation for acquiring this sweet reward was tested using the PR operant schedule. In this test, as in the previous sensitivity test protocol, the mice were able to choose between the saccharin solution and plain water at each corner, but the following rules were added: After the tasting trial, mice were intially required to make two consecutive nosepokes to receive a 4000 ms drink of either saccharin water or plain water, at the beginning of the effort-based choice task. Thereafter, each time the total number of preference-based choices exceeded 50, the number of nosepokes required to drink saccharin water was increased one by one until 10 nosepokes were required for mice to obtain an opportunity to drink saccharin water. During this period, the rates of preference-based choice for saccharin water to total preference-based choice was used in the analysis as an index of motivation to seek palatable pleasure.

QUANTIFICATION AND STATISTICAL ANALYSIS

Imaris software was used for pre-synaptic and post-synaptic *puncta* detection and confocal fluorescence microscopy images processing. Pre-synaptic and post-synaptic spots were colocalized using a MATLAB colocalization script (Colocalize Spots XTension). Data visualization and statistical analyses were performed using GraphPad Prism 10 (ver. 10.4.1). All statistical data were presented with error bars indicating the standard deviation (SD), with details provided in each figure legend. Semi-quantification of western blot results was performed using ImageLab software (Biorad).